# UAV survey in volcano-tectonics: Methodology, best practice and application to the Iceland rift

*Bonali F.L.[1], Tibaldi A.[1], Marchese F.[1], Fallati L.[1], Russo E.[1], Corselli C.[1], Savini A.[1]*
*[1] Department of Earth and Environmental Sciences, University of Milan-Bicocca, Milan, Italy*

*[*]Corresponding author: Dr. Fabio Bonali, Department of Earth and Environmental Sciences, University of Milan-Bicocca, P. della Scienza 4, 20126, Milan, Italy; e-mail: fabio.bonali@unimib.it, tel. +39 0264482066*

**Abstract**

In the present work, we tested the use of an Unmanned Aerial Vehicles (UAVs) - quadcopter - and the Structure from Motion (SfM) digital photogrammetry image processing technique for volcano-tectonics and active tectonics studies. Systematic tests were developed with different flight configurations, in order to measure the amount and direction of opening of tension fractures and the height of active fault scarps in the Theistareykir Fissure Swarm (ThFS), a rift in the Northern Volcanic Zone of Iceland. Detailed geological-structural field surveys were carried out in the same areas surveyed by UAV in order to assess accuracy of the UAV data and the associated reliability of this approach. Our results indicate that 100 meters is the most efficient UAV flight elevation for data collection, taking into account: *i)* data quality and accuracy; *ii)* number of collected data; *iii)* areal coverage extension; *and iv)* battery duration. By using Aerial Structure from Motion (ASfM) technique, we collected 361 structural data that allowed us to reconstruct, within the studied rift, an overall spreading direction of N108° during Holocene times, which has been compared with geodetic motion vectors, and we also calculated a stretch of 1.013 regarding 8-10 ka old lava units. Deformations in the area are related to both dyke intrusions and extensional tectonics.

Keywords: UAV; Fracture; Rift; Spreading direction; Iceland.

**Highlights:**

- We studied Holocene deformations within the Northern Volcanic Zone of Iceland

- Normal faults and tension fractures have been studied by field and UAV surveys
- We defined the geometry of 397 fractures and collected 361 structural data
- The overall spreading direction of the area has been reconstructed by UAV survey
- We suggest a new standard for UAV surveys for studying volcano-tectonic features

## 1. Introduction

Earth objects of interest for volcano-tectonic and active tectonic studies are mainly represented by joints, open fractures (here termed tension fractures), faults and folds (e.g. Gudmundsson, 1987; Cembrano and Lara, 2009; Tadini et al., 2014). Joints are usually a few meters to some tens of meters long, tension fractures can be kilometres long, folds and faults can be tens of kilometres long (e.g. Tibaldi and Bonali, 2018). The large dimension of faults attracted the attention on the use of images from satellite platforms to detect "lineaments" since the 80' yrs. Hundreds of papers and books have been published on the best practice to detect and analyse geologic lineaments by satellite remote sensing (e.g. Wise et al., 1985; Marino and Tibaldi, 1988; Tibaldi and Ferrari, 1991; review in Ramli et al., 2010). Space-borne remotely-sensed images had a series of revolutionary aspects, such as the synoptic plan view, extremely useful to gain the whole perception of long linear geological features, combined with global coverage, time repetition, and the possibility of selecting a wide spectrum of sensors with different resolution and wavelengths. However, space-borne remote sensing platforms present also a series of limitations: it is impossible to plan a survey on specific dates and time, resolution has been improved in the recent-most sensors but can still be too poor for some specific target, and high-resolution data are too expensive to cover the study of large-scale geological features.

On the contrary, Unmanned Aerial Vehicles (UAVs) are becoming more and more popular also for scientific purposes, thanks to a series of characteristics that make them more competitive and useful than satellites: *i)* allow to choose appropriate data acquisition and time; *ii)* it is possible to adjust flying height, and obtain very high spatial resolution; *iii)*

can repeat flights daily or several times per day; *iv)* it is easy to produce three-dimensional models of terrains; *v)* it is possible to survey also vertical rock cliffs; *vi)* the cost of data acquisition is substantially lower than that of high-resolution satellite imagery; *vii)* UAVs can carry various types of sensors designed for specific purposes.

Regarding geological hazards, UAVs have been recently used to monitor the urban damaged zones after earthquakes (Baiocchi et al., 2013) and landslides (Gong et al., 2010; Hu et al., 2012; Rathje and Franke, 2016), as well as to detect deformations occurred during volcanic eruptions (Müller et al., 2017; Darmawan et al., 2018) and along lava flows (Favalli et al., 2018). UAVs have also been crucial for studying geysers and hot springs at the Geysir geothermal field, southern Iceland (Walter et al., 2018).

After the first attempts with balloons (Johnson et al., 2014), some specific works are appearing in the very recent literature, where UAV-based imagery is also used to map active faults (Angster et al., 2016; Deffontaines et al., 2016; Jiao et al., 2016; Bi et al., 2017; Gao et al., 2017; Wu et al., 2017). Anyway, the number of works dealing with this application of UAV imagery is still very limited and thus this type of research method can be considered to be in its infancy, but with a great potential for future prospects. More important, the aforementioned works are more focused on describing the structural characteristics of the site of investigation than on the assessment of the method variables and consequent inaccuracies. Only Bemis et al. (2014) suggested that UAV-based surveys useful for structural geology can be carried at altitudes of 30-40 m, which produce high resolution imagery with 1 pixel = 1 cm. They also indicated that altitudes of 15-20 m can allow to reach sub-cm resolutions, although this is countered by larger datasets and associated increase in data processing time.

Based on the above, there is an important lack in assessing and describing the best practice in the use of UAVs for active tectonics and volcano-tectonic studies, and thus it is scientifically necessary to improve our knowledge on this application of UAVs. Our study deals with surveying, for the first time by UAVs, active faults and tension fractures, which

are formidable structural features to reconstruct the present strain field of wide areas, based on the measurement of the opening vectors along the fracture margins. Usually this is done by time-expensive fieldwork (e.g. Pasquarè Mariotto et al., 2015; Tibaldi et al., 2016a, b), whereas UAV surveys may help to quickly measure fracture opening over wide areas. This method is crucial especially in case of logistically difficult terrains, where it is impossible to directly reach important geological features. In the present paper, we thus contribute by a methodological approach to answer to the following challenging questions: *i)* which is the best height at which an UAV must fly in order to obtain useful images of active structural objects of different dimensions, compatibly with parameters such as time and resolution? and *ii)* may UAV surveys be used to reconstruct with enough detail the tectonic strain field? By replying to the first answer, we can suggest how to plan UAV flights by choosing the elevation *a priori*. Furthermore, it is of paramount importance to identify the precision of these measurements especially when dealing with very small features, such as piercing points at tension fractures, necessary in reconstructing the strain field. In line with the above, we tested two different altitudes for UAV surveys (Figs. 2A-B) and then we compared the results with detailed field studies of the same areas. Both UAV and field approaches have been applied to quantify fault scarp height and the amount and direction of opening at active tension fractures. The work has been carried out in the Theistareykir Fissure Swarm (ThFS) in the Northern Volcanic Zone (NVZ), Iceland (Fig. 1), where this kind of studies is also important to contribute to the assessment of local seismic and volcanic hazards. Finally, we reconstructed the active strain field of a wide area within the northern Iceland rift and compared results with other geophysical data such as geodetic measurements.

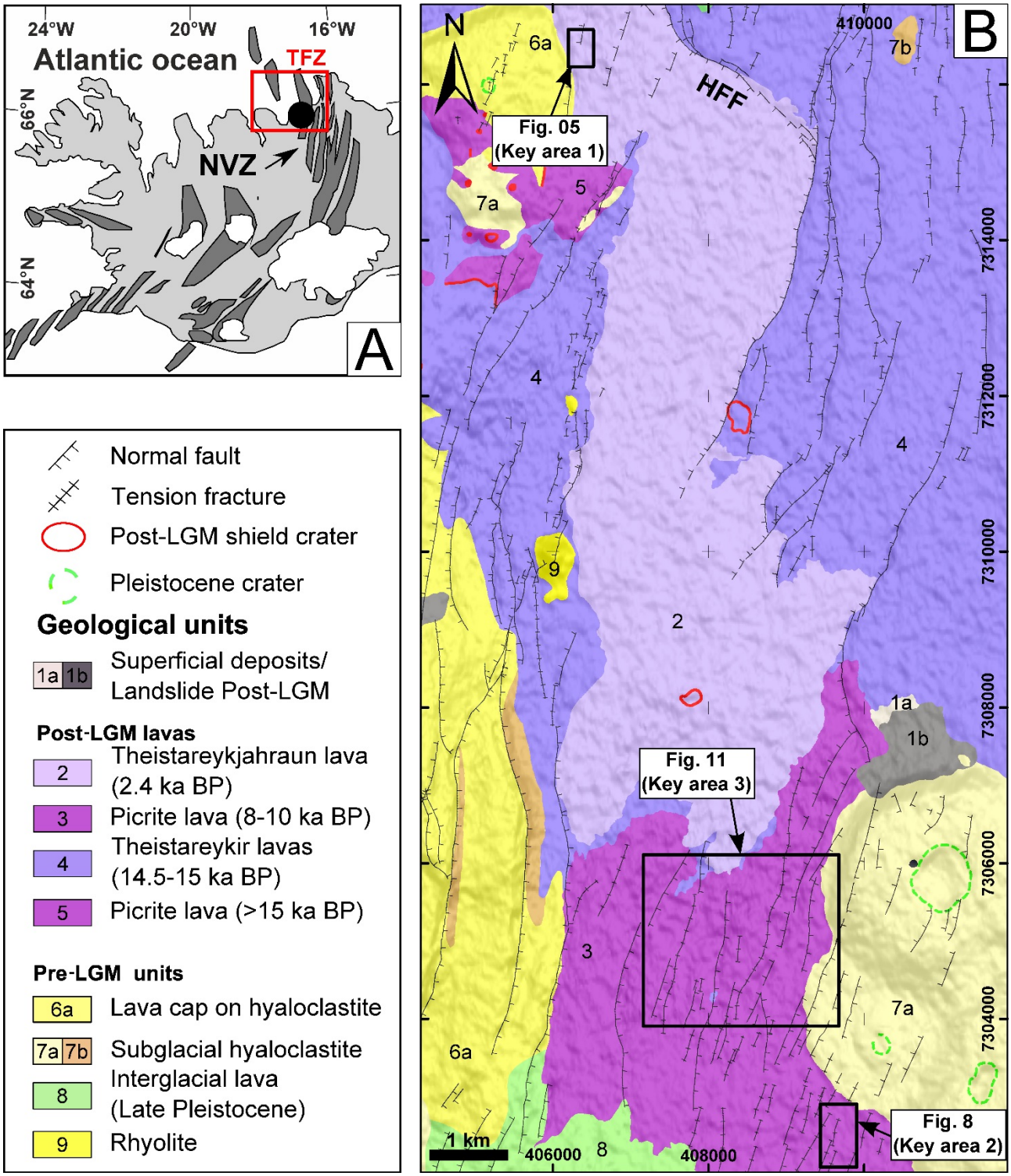


***Figure 1.*** *(A) Inset with location of study area. NVZ = Northern Volcanic Zone. TFZ = Tjornes Fracture Zone. (B) Geological map of the study area based on Saemundsson et al. (2012). Key areas are indicated as black rectangles. Figures 5, 8 and 11 are located.*

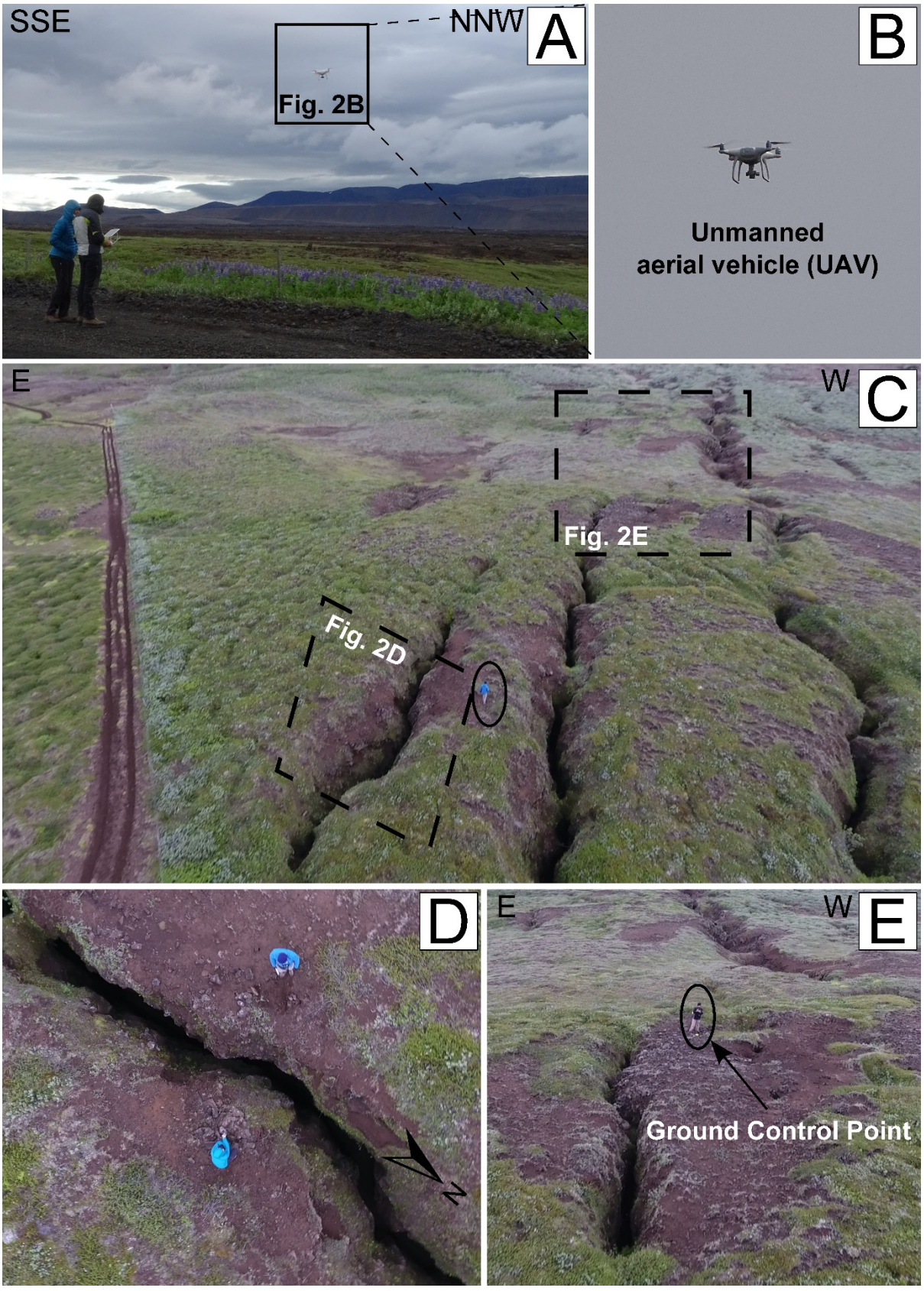


***Figure 2.*** *(A) UAV surveying the rift zone of Iceland and operators at work. (B) Our DJI Phantom 4 quadcopter in action. (C) View from UAV survey of the tension fracture field located in Key area 1. Man for scale (black circle). (D) UAV view of a tension fracture, location is shown in Figure 2C. Persons for scale. (E) Operator is positioning a Ground Control Point (GCP) in the study area. Location is shown in Figure 2C.*

## 2. Methods

### 2.1 Key areas selection

In our study, we selected three key sites within the ThFS (Fig. 1B) to test UAV approach, since they are characterized by the presence of well exposed Holocene normal faults and tension fractures (Pasquaré Mariotto et al. 2015; Tibaldi et al., 2016a) that have been also surveyed by fieldwork. These areas, named as Key areas 1, 2 and 3, are characterized by lava flows of different ages (2.4 and 8-10 ka old, respectively, Saemundsson et al., 2012) and structures with different dimensions*: i)* the recentmost lavas (Key area 1) are affected by normal faults and tension fractures, with very small dilation (a few dm); *ii)* older lavas (Key area 2 and 3) are affected by several tension fractures with dilation values generally > 40 cm. A clear example of tension fractures that have been surveyed is shown by the screenshots in Figs. 2C-D-E, which are located in Key area 2.

Key areas 1 and 2 have been tested by collecting field data and by measuring structures on UAV-resulting orthomosaics and Digital Terrain Models (DTMs). UAV flights at the origin of orthomosaics and DTMs have been performed at altitudes of 50 m and 100 m, in order to choose the most suitable flight elevation for collecting the best-quality data for volcano-tectonic purposes, taking into account different aspects: *i)* number of surveyed features; *ii)* time of flight; *iii)* level of accuracy. Finally, we completed UAV surveys in Key area 3, located within the 8-10 ka old lava (Fig. 1B) that has never been studied before, to contribute to the understanding of the ThFS tectonic evolution.

### 2.2 UAV selection and use

UAVs can be subdivided into fixed-wing types, which recall model airplanes, multi-rotor types and balloons. While balloons do not need fuel or a battery, on the other hand they cannot be remotely controlled. Fixed-wing UAVs can cover very large areas in a smaller timeframe respect to multi-rotor UAVs and consume less energy. Nonetheless, multirotor UAVs have important advantages especially for high-resolution studies, because they can

fly also at very low altitudes attaining a greater field resolution in terms of pixel size respect to fixed-wing UAVs. Moreover, small multirotor UAVs, as the one used in the present work, can offer a good cost-effective solution for short-range surveys. For these reasons, we tested the multi-rotor platform, and specifically a quadcopter, which is the most used and versatile UAV.

We used the DJI Phantom 4 quadcopter (Figs. 2A-B), which surveyed Key areas 1, 2 and 3 in time consecution in order to take data under the same sun orientation and elevation. The DJI Phantom 4 is equipped with a high-quality camera, capable of recording 4K videos at 30 fps, supports micro SD card with a maximum capacity of 64 GB, and, much more importantly, it was chosen for its long flight time (≈ 28 min). Photos are shot at 12.4 Megapixels, including EXIF information (Exchangeable image file format) and GPS coordinates, a level of resolution and a set of information that are essential for research purposes. Thanks to a built-in high precision 3-axis gimbal, flights are smooth and the collection on the images is stable. Furthermore, the DJI Phantom 4 provides constantly stable flights thanks to the integrated GPS system, including position holding, altitude lock and stable hovering. Further main characteristics of this quadcopter are summarized in Table 1.

In order to accurately georeference the key areas imagery, real-world coordinates of, at least, four Ground Control Points (GCPs) have been established within each surveyed area (e.g. James and Robson, 2012; Turner et al., 2012; Westoby et al., 2012). For each key area, we placed well visible target markers (e.g. Fig. 2E, Figs. 4B-C) that were surveyed using dual frequency differential GPS.. Obviously, the targets for the areas surveyed at different altitudes are the same, in order to have a good match of the resulting orthomosaic and DTM. UAV-captured photos have been collected in order to have an overlap of 90% and have been processed with the use of Agisoft PhotoScan (http://www.agisoft.com/), a Structure from Motion (SfM) software. The SfM technique allowed to identify matching features in different images, collected along a defined fly path (Fig. 3B), and combine them

to create a sparse and dense cloud (Figs. 3C-D), a mesh, an orthomosaic and a DTM as final products (further details in Stal et al., 2012, and Westoby et al., 2012). The workflow for model reconstruction is shown in Figure 3A.

***Table 1.*** *Main features of DJI Phantom 4 quadcopter.*

| | |
|---|---|
| **Name** | Phantom 4 |
| **Release Date** | March 2016 |
| **Weight** | 1380 g |
| **Max Speed** | 20 m/s |
| **Battery** | 5350 mAh LiPo 4S |
| **Max Ascent Speed** | 6 m/s |
| **Max Descent Speed** | 4 m/s |
| **Max Flight Time** | 28 min |

***Table 2.*** *Details regarding UAV surveys at different altitudes and photo collection.*

| Area | Flight altitude (m) | Areal coverage ($km^2$) | Nr. of photos | Flight time (':") | DTM resolution | Orthomosaic resolution |
|---|---|---|---|---|---|---|
| Key area 1 | 100 | 0,03 | 40 | 4:39 | 8 cm/pixel | 8 cm/pixel |
| Key area 1 | 50 | 0,03 | 159 | 7:38 | 2 cm/pixel | 2 cm/pixel |
| Key area 2 | 100 | 0,054 | 81 | 4:25 | 8 cm/pixel | 8 cm/pixel |
| Key area 2 | 50 | 0,054 | 208 | 8:37 | 2 cm/pixel | 2 cm/pixel |
| Key area 3 | 100 | 2,525 | 3027 | 126:20 | 8 cm/pixel | 8 cm/pixel |

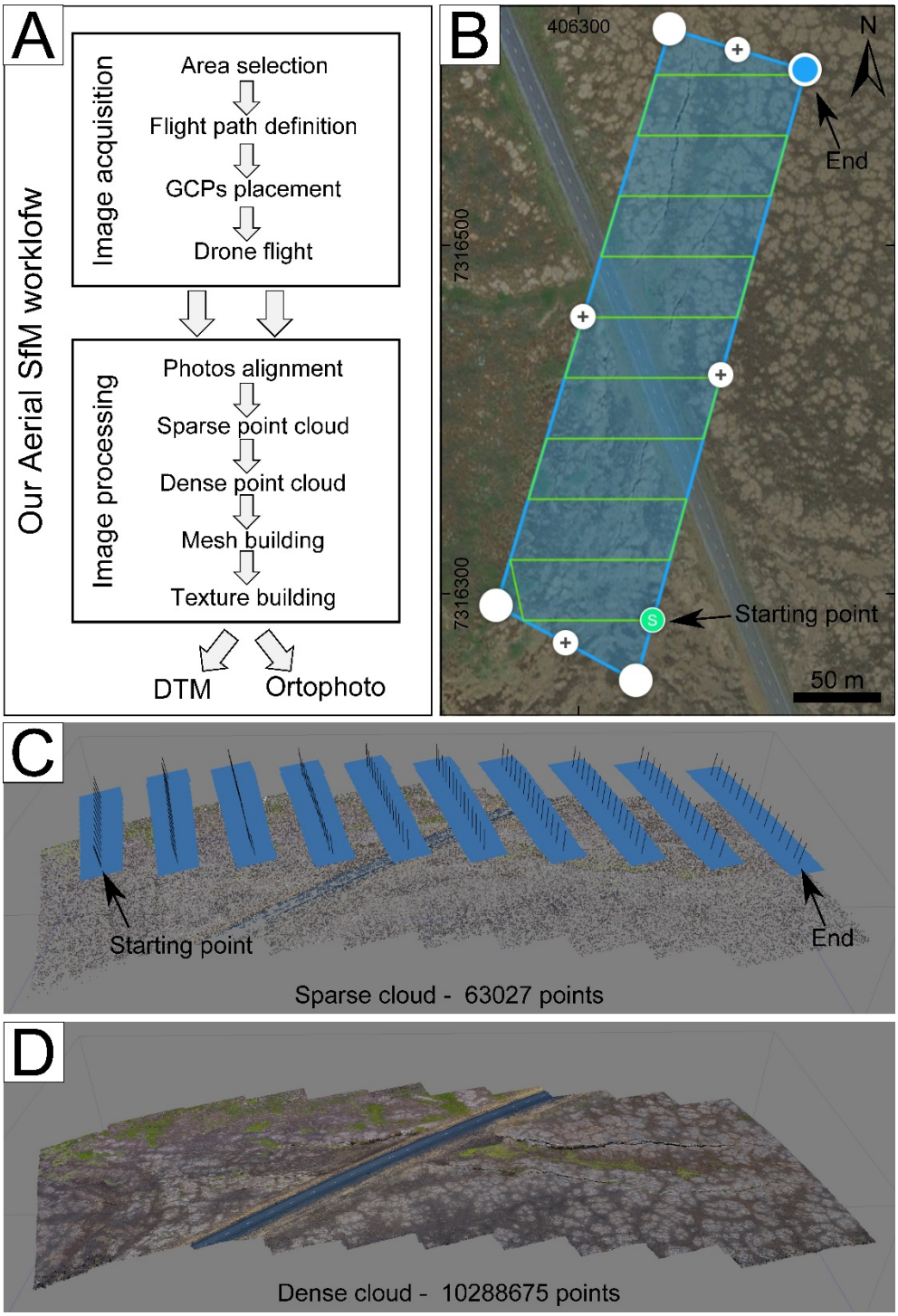


***Figure 3.*** *(A) Workflow used in the present research to generate DTMs and orthomosaics using AgiSoft Photoscan. (B) UAV flight path (green line) over Key area 1, at 50 m of altitude. Blue square indicates the surveyed area. Sparse (C) and dense (D) cloud generated by Agisoft Photoscan. Computed camera positions are represented as blue rectangles, black lines show the pitch angle and photo orientation.*

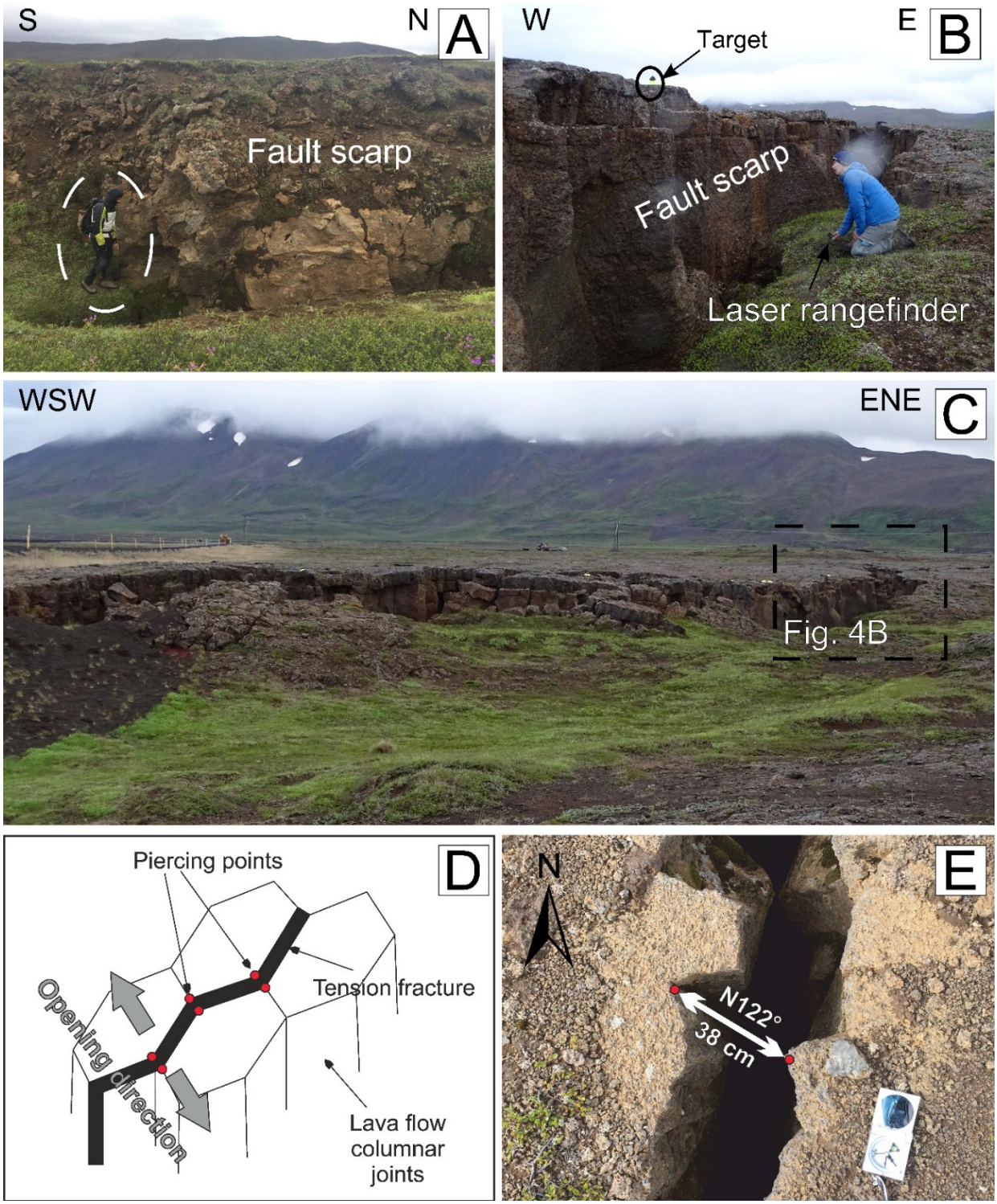


***Figure 4.*** *Examples of vertical fault scarps measured in the field and by UAV surveys affecting the 8-10 ka (A) and 2.4 ka old lavas (B-C), respectively. Location of Figure B is shown in Figure 4C. (D-E) Sketch and field example of a tension fracture showing clear piercing points that indicate the vector of fracture opening, also the amount of dilation has been quantified.*

### 2.3 Data collection and comparison

For Key areas 1 and 2, we firstly collected field measurements of faults and tension fractures and then we remotely measured the same points on orthomosaics and DTMs. The vertical component of fault offset has been measured in the field by tape and/or laser rangefinder (Figs. 4A-B), whereas on DTMs it has been quantified by measuring the difference in altitude along a topographic profile traced orthogonally to the fault scarp (insets in Figs. 5C-D, 8C and 8D). Another geological feature that has been both field- and UAV-measured is the amount of dilation and the opening direction of tension fractures: due to the presence of lava flow columnar joints, which guided fracture opening, the operator is able to take these measurements in correspondence of piercing points on each side of the tension fracture (sketch in Fig. 4D and field example in Fig. 4E). These values have been measured by compass and laser rangefinder in the field, or by tracing a line connecting the piercing points on orthomosaics and calculating dilation and opening direction in GIS environment. A clear field example is shown in Figure 4E: in this case, the fracture is characterized by visible piercing points that allow to quantify an opening direction of N122° and an amount of opening of 38 cm. Whenever a continuous vertical offset (with a minimum of 1 m) has been detected in correspondence of tension fractures in the field, the opening direction and amount of dilation have not been quantified, in order to avoid errors, such as overestimations, due to gravity effect. Furthermore, in the cases where piercing points were not clearly visible, the dilation has been measured perpendicularly to the fracture strike. Data have been also collected for Key area 3 with the same approach and all three areas have been compared for better defining the UAV methodology.

## 3. Geological-structural background of the key areas

The NVZ, where the areas of test are located, is situated in the north-eastern part of Iceland and represents the northernmost point where the Mid-Atlantic Ridge emerges. The NVZ is connected to the Kolbeinsey Ridge (KR) through the Tjornes Fracture Zone and is

composed of five, about N-S-striking, volcanic rift zones, where the ThFS is the westernmost (Fig. 1A; Hjartardòttir et al., 2016b). The ThFS is dissected by the NW-SE-striking Husavik-Flatey transform fault (HFF), which is characterized by dominant dextral strike-slip movements. ThFS consists of 8 km-wide and 34 km-long swarms of N-S to NNE-SSW-striking fractures that can be classified as: *i)* normal faults (shear fractures with dominant vertical component), with evident scarps resulting from large dip-slip offset (up to tens of meters); *ii)* tension fractures (extensional structures with negative least principal stress $\sigma_3$), which show clear opening direction and amount of opening; and *iii)* eruptive fissures. These structures tend to be parallel each other apart from the site of interaction between the ThFS and the HFF, where they rotate anticlockwise and reach a N-S to NNW-SSE strike (Gudmundsson et al., 1993; Fjäder et al., 1994; Magnusdottir and Brandsdottir, 2011; Pasquaré Mariotto et al., 2015; Hjartardóttir et a., 2016b; Tibaldi et al., 2016a, 2016b).

Our key sites are located in lava units of 2.4 ka (Key Area 1) and 8-10 ka (Key areas 2 and 3) BP respectively, affected by normal faults and tension fractures (Fig. 1B). At a general level, in the ThFS there is a wide range of depositional units represented by volcanic and sedimentary sequences of Miocene to Pleistocene age, and lava flows of Pliocene, Pleistocene and Holocene age (Saemundsson, 1974; Garcia et al., 2002). We have chosen of focusing our surveys on Holocene units to better recognize and study evidences of tectonic and volcano-tectonic activity without any perturbation due to abrasion of glaciers during the Late Glacial Maximum.

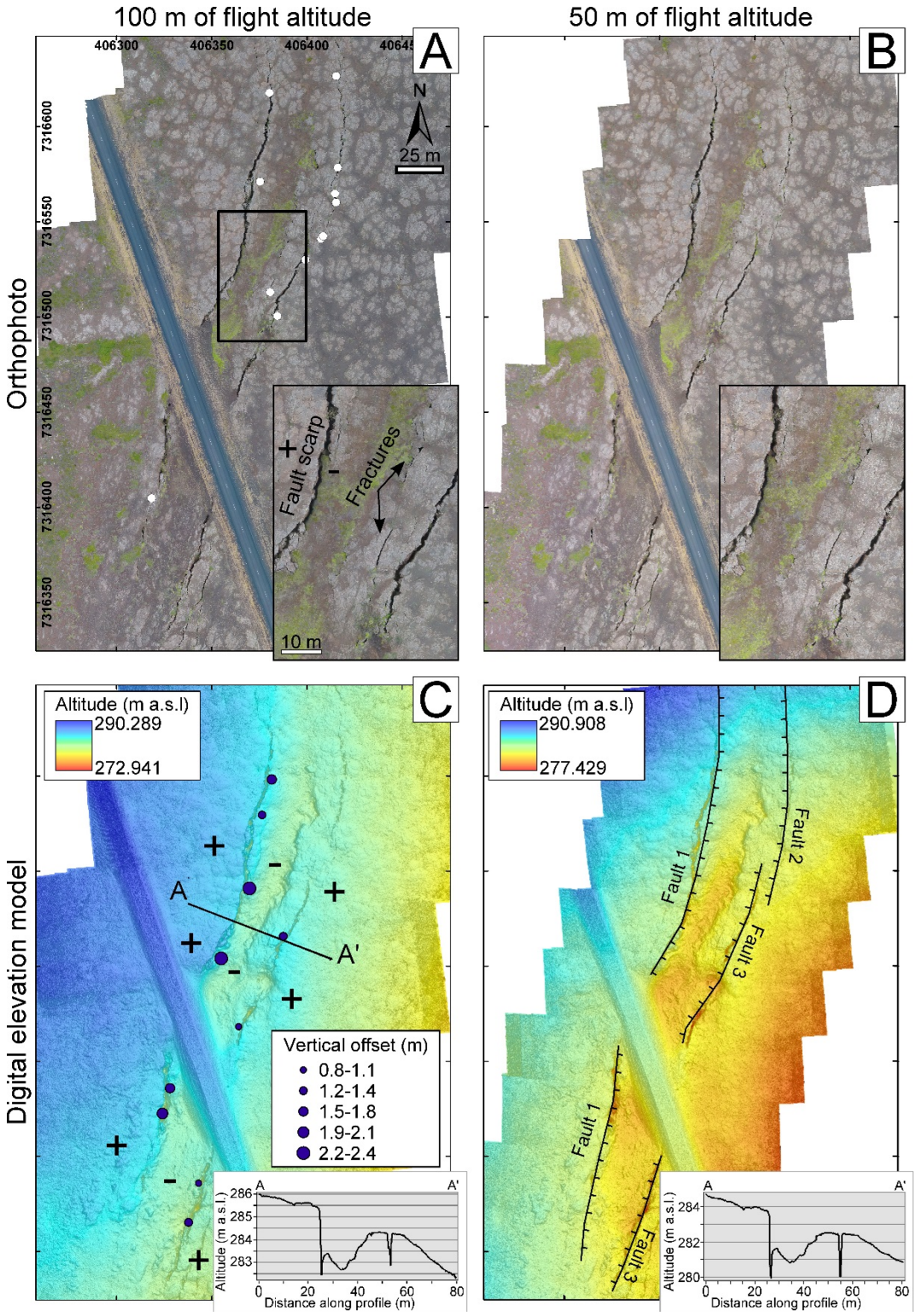


***Figure 5.*** *Orthomosaics (A-B) and Digital Terrain Models (C-D) of Key area 1 from UAV surveys at an elevation of 100 m (A-C) and 50 m (B-D) respectively. In the lower right corner of Figures 5A and 5B, same detail of fracture field and fault scarps. In the lower right corner of Figures 5C and 5D (DTMs), same topographic profile A-A' is represented. '+' and '-' symbols represent uplifted/subsided blocks. Altitudes are shown as a colour range (legend in figure). White dots in Figure 5A and purple dots (scaled with vertical offsets) in Figure 5C represent 10 stations of field measurements. Figure 5D contains faults n.1, 2 and 3; slip profiles of these faults are shown in Figure 6G.*

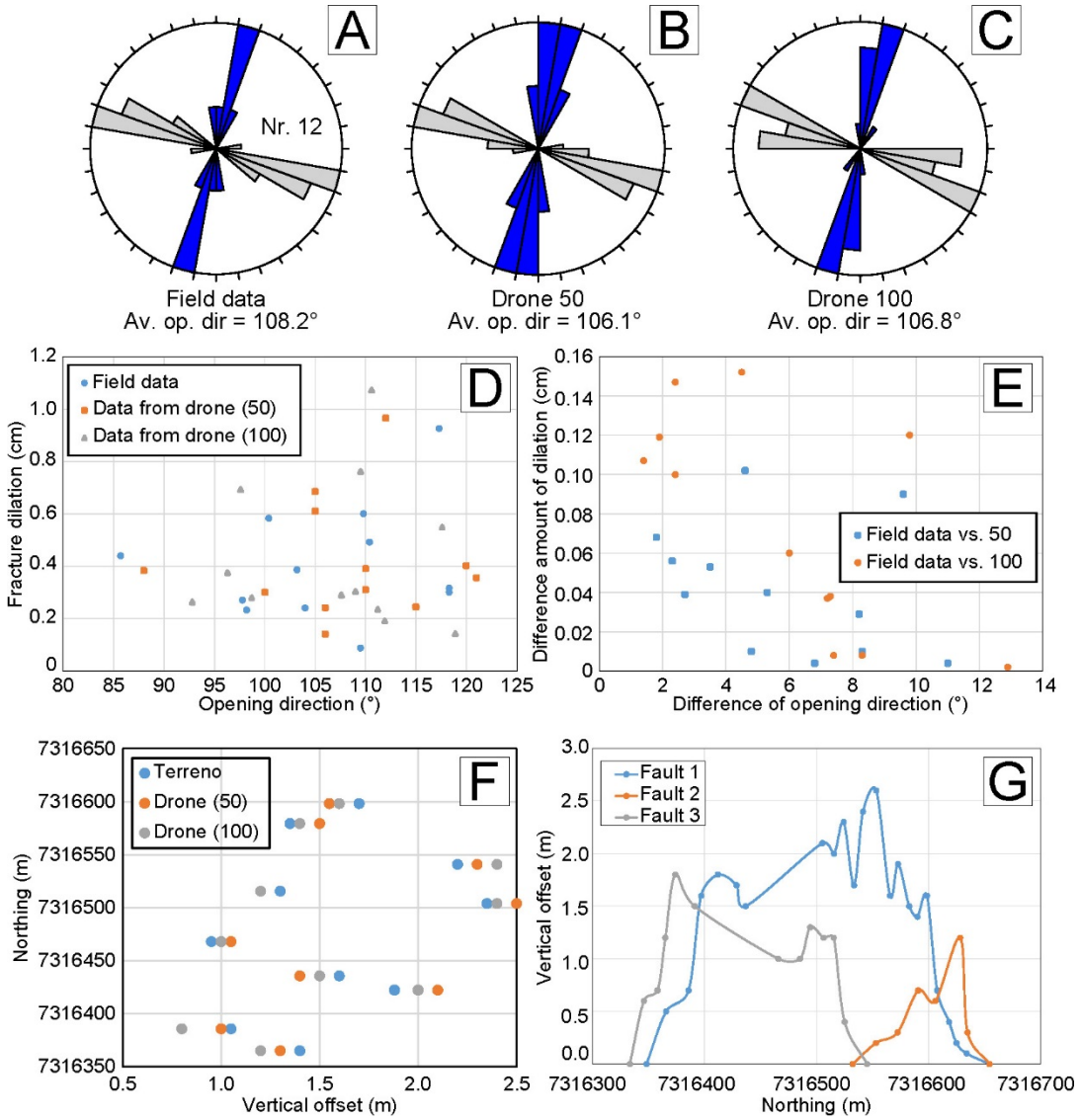


***Figure 6.*** *Rose diagrams showing strike (blue) and opening direction (grey) of tension fractures measured in the field (A), and on orthomosaics from UAV surveys at an elevation of 50 m (B) and 100 m (C). (D) Opening direction vs. fracture dilation for field data and UAV surveys at both elevations. (E) Difference of opening direction vs. difference in amount of dilation between field-acquired data and flight surveys at both elevations. (F) Vertical offsets measured in the field and by UAV surveys at both elevations. (G) Slip profiles of fault scarps located within the graben located in Key area 1: vertical offsets have been remotely measured on the DTMs. Faults are located in Figure 5D.*

## 4. Results

The UAV surveys allowed producing orthomosaics and DTMs of each key area via SfM technique, details are summarized in Table 2. In the following sections, we firstly present the results for Key areas 1 and 2, used to choose the most useful and efficient flight altitude, and then results for Key area 3.

### 4.1 Key area 1

Figures 5A-C show the orthomosaics and DTMs of Key area 1, obtained from the 100-m-high UAV survey with a resolution of 8 cm. The inset in the lower right corner of Figure 5A highlights very well visible fractures and a fault scarp, while the inset in Figure 5C is the topographic profile A-A', traced orthogonally to the graben. The same area has been surveyed with a flight elevation of 50 m and a resulting 2 cm resolution: results are shown in Figures 5B-D. The area is characterized by the presence of two main normal faults striking NNE-SSW affecting the 2.4 ka old lava: two scarps face to the WNW and one to the ESE, mimicking a graben morphology that is about 30 m large. The eastern fault can be divided in two different segments (Fault n. 2 and 3 in Fig. 5D). The main faults that outline the graben morphology (Fault n. 1, 2 and 3) are shown in Figure 5D: we assume that faults 1 and 3 continue beneath the road to the southwest. Several tension fractures are also present. As shown in the DTMs (Figs. 5C-D), the western part of the area has a general altitude higher than the eastern part and the central part of the graben is always located in the collapsed area. Furthermore, the western block of the graben is higher than the eastern one, as shown in the topographic profiles. Vertical offset of scarps has been measured at several points in the field (Fig. 5C), resulting in a maximum vertical offset of 2.35 m for the western part and 1.4 m for the eastern. Such data have been compared to the vertical offset obtained by DTMs resulting from UAV survey (Fig. 6F): the difference in vertical offset is always in the range of 0.05-0.25 m, whereas averaged difference is equal to 0.13 m (st.dev. = 0.05) and 0.12 m (st.dev. = 0.07) (elevation of 50 and 100 m respectively).

We also surveyed tension fractures in order to collect and compare fracture dilation and opening direction measured in the field at 17 sites with measurements remotely quantified on orthomosaics from UAV surveys. Rose diagrams from field data and from UAV surveys reveal N-S to NNE-SSW-striking fractures (Figs. 6A-B-C), with opening directions ranging from N88° to N121° (Fig. 6D) and dilation ranging from 0.14 m to 1.07 m (Fig. 6F).

Much more importantly, averaged opening direction is always between N106° and N108° and the difference between averaged values measured in the field and with the UAV (considering both 50 m and 100 m of flight altitude) is just 1.9° and 1.4°, respectively. More in detail, tension fractures show an average difference of measured dilation (between UAV and field data) of 0.04 m (st. dev. = 0.03) in the case of 50-m-high and 0.07 m (st. dev. = 0.05) in case of 100-m-high UAV surveys. The difference in opening direction is equal to 5.7° (st. dev. = 3.0) in the first case and 6° (st. dev. = 3.6) in the latter case (Fig. 6E). Moreover, the differences between measures of vertical offsets are shown in Figure 6F: there is no clear tendency to overestimate or underestimate measures if comparing field activity and UAV surveys.

By comparing field data with UAV data, we found out a good match both regarding fault vertical offsets and fracture dilation/opening directions. As a consequence, we present a complete survey for Key area 1 through 52 measurements of fractures (Fig. 7A) and providing offset profiles of faults from the 100 m elevation orthomosaic (Fig. 6G). Our results suggest that the overall fracture strike in this area is N18.9°, while the opening direction is N108.1° and the averaged fracture dilation is 0.38 m (Fig. 7A). Dilation values range from 0.09 m to 1.21 m. These values have been calculated only related to fractures that have not been affected by erosion, with a limited (or null) amount of sediments and with no fallen rocks on their sides: all these are factors that might alter the final measurement and that must be avoided to reach accuracy. The whole set of 69 fractures is reported as a sketch in Figure 7B: all of them, mostly striking N-S, have been traced on the orthomosaic generated by the 100 m elevation UAV survey.

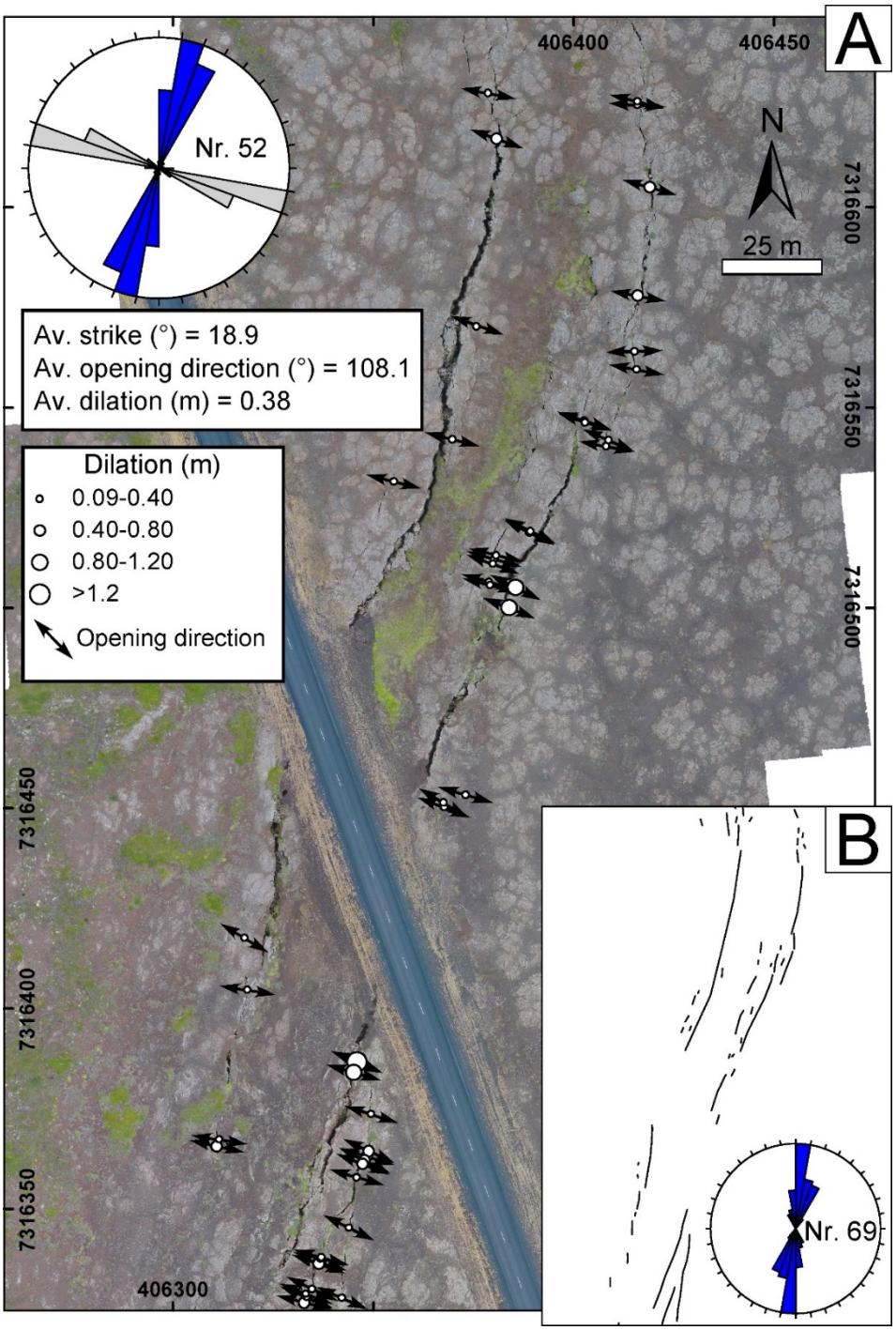


***Figure 7.*** *(A) Fracture dilation (in meters) and opening direction measured on the 8-cm-resolution orthomosaic, related to a UAV survey at 100 m in Key area 1. A total of 52 measures have been taken, as shown by the rose diagram in the upper left corner. Fracture strike (represented in blue in the rose diagram), opening direction (represented in grey in the rose diagram) and dilation (in meters) are reported, also as averaged values. (B) Sketch of fractures traced on the 100 m elevation orthomosaic of Key area 1. Rose diagram shows strike values (69 total measures).*

### 4.2 Key area 2

Figures 8A and 8C, which are related to the survey of Key area 2 at an elevation of 100 m, represent the resulting 8 cm resolution orthomosaic and DTM, whereas Figures 8B and 8D are related to the 50 m-high survey, with a resulting resolution of 2 cm. The inset in the lower right corner of Figures 8A and 8B, which represents the same area, allows to appreciate the level of detail of surveys at each elevation. At a general level, the area is characterized only by NNE-SSW-striking tension fractures that affect 8-10 ka old lava units (Fig. 10B). Altitude of the area is lower to the south and to the north respect to the central part (Figs. 8C-D). Furthermore, the topographic profile A-A' shown in Figures 8C and 8D highlights the presence of a bulging of the topographic surface, of about 2 m, in correspondence of the tension fractures, possibly related to the presence of a dyke beneath them (review in Tibaldi, 2015). The lighter colour that can be seen inside the tension fractures in Figure 8D, which is related to the 50-m-high survey, reveals that the lower the elevation of the survey, the higher the possibility to reach deeper levels of fractures. Since the good match between field and UAV data regarding the opening direction and dilation has been already demonstrated for Key area 1, here we show a different example.

We present a comparison between different methodologies to accurately measure the amount of opening and opening directions of tension fractures (Figs. 9A-B-C). Although the resolution of the satellite image (Fig. 9A) is very high (50 cm – image from Worldview-2 sensor, Catalogue ID 1030050051F92D00), it is not enough to provide accurate quantitative measures of opening directions, and thus it does not represent a valid alternative to field measurements. Differently, orthomosaics from UAV surveys at different altitudes (100 m and 50 m, Figs. 9B and 9C respectively) are suitable to trace the line connecting piercing points along the fracture representing the opening vector, which is characterized by a direction and *modulo*. In both cases, opening vectors have been traced by the same operator and using the same methodology: on the best-resolution orthophoto, associated

with 100-m-high survey (Fig. 9C), it has been possible to recognize and measure 7 opening vectors, only one more than in the orthophoto in Figure 9B. Figure 9D represents a scatter plot of opening direction versus fracture dilation measured on the 100-m-high (orange dots) and 50-m-high (blue dots) orthomosaics.

Furthermore, since dilation and opening direction quantifications are almost the same in both orthomosaics, even though they have different resolutions, we conclude that a flight altitude of 100 m provides already reliable results for studying these geological features. As a consequence of the above, 34 measures have been taken from the 100 m orthomosaic (Fig.10A) , resulting in: *i)* fracture dilation values ranging from 0.5 to 2.5 m; *ii)* average strike of fractures is N12.7°; *iii)* average opening direction is N108°; and *iv)* average fracture dilation corresponding to 1.44 m. Fractures belonging to this area (total of 68) have also been traced by hand on the 100-m-elevation orthomosaic (Fig. 10B): according to the rose diagram, they strike in the range N-S to NNE-SSW.

A further consideration arises: in the field, an operator can be inclined to measure the amount of opening of fractures as the distance between the fracture rims. Anyway, processes of erosion due to gravity, or cryoclastims, or a combination of them, can enlarge the fracture near the topographic surface (white dashed line in Figs. 9E-F). This creates a funnel-shaped profile and, as a consequence, an overestimation of the dilation amount. A correct measurement should imply the reaching of a deeper level inside the fracture, in order to arrive to the original fracture walls (white line in Figs. 9E and 9F). Here, a correct measurement by a field operator can be done (e.g. Fig. 9E) only if this level is reachable. We observed, instead, that the UAV images allow to distinguish the area enlarged for erosion respect to the original fracture geometry (Fig. 9F), and thus the view from above allows to quantify more correctly the dilation amount.

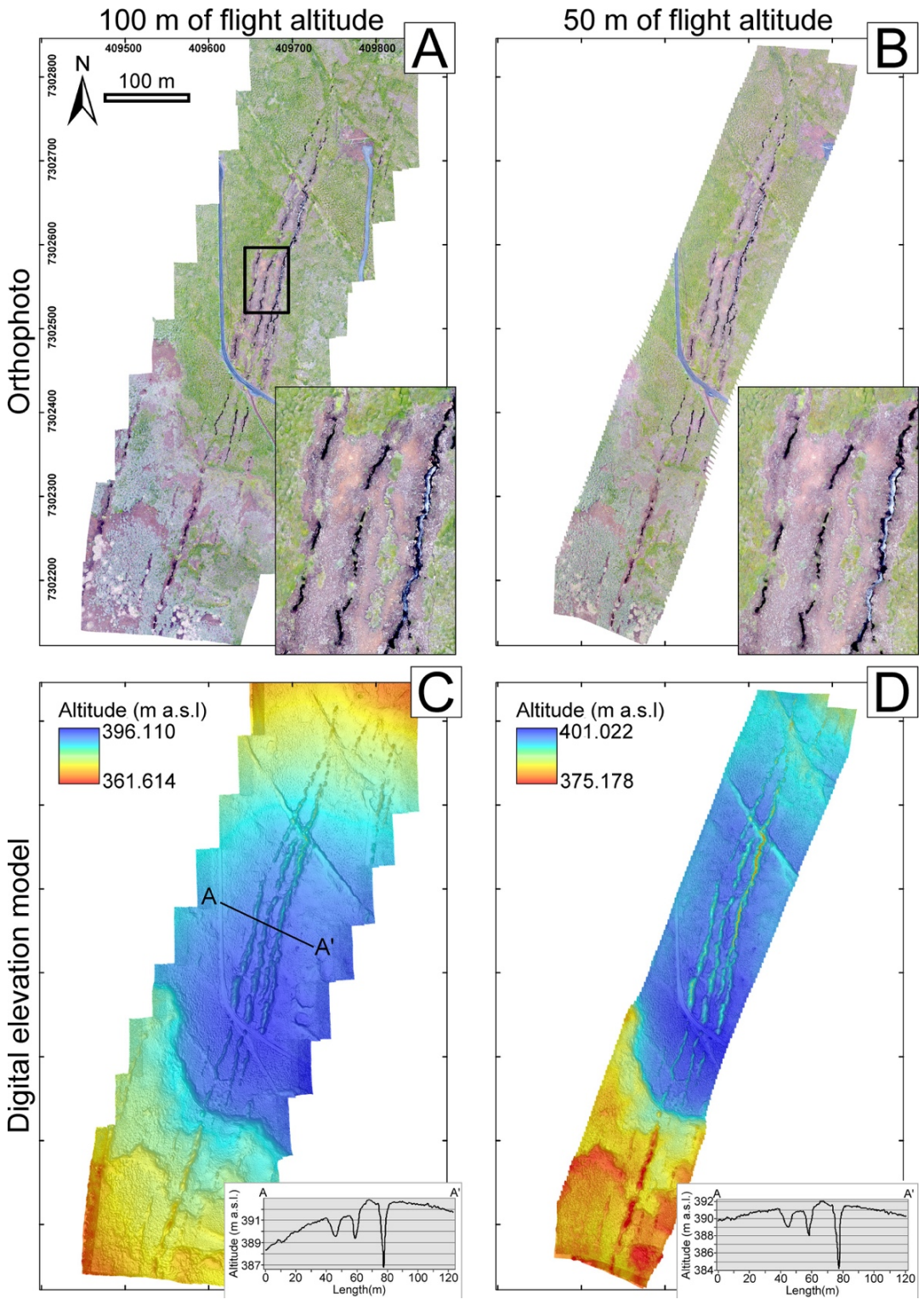


***Figure 8.*** *Orthomosaics (A-B) and Digital Terrain Models (C-D) of Key area 2 from UAV surveys at an elevation of 100 m (A-C) and 50 m (B-D), respectively. In the lower right corner of Figures 8A and 8B, same detail of fracture field. In the lower right corner of Figures 8C and 8D (DTMs), same topographic profile A-A'. Altitudes are shown as a color range (legend in figure).*

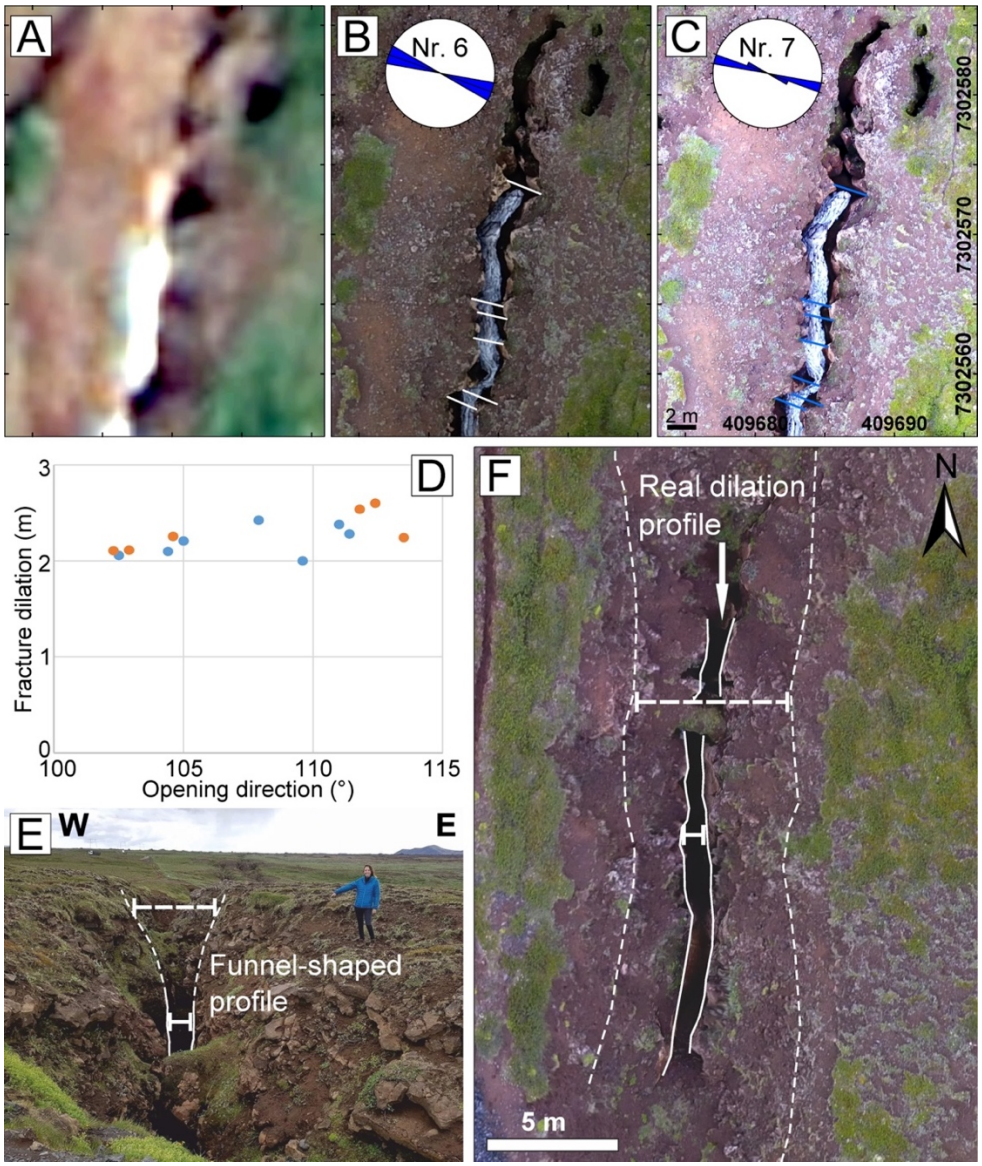


***Figure 9.*** *(A) Orthophoto from satellite view (0.5 m resolution) belonging to the Key area 2 characterized by 8-10 ka old lavas. Layout in area 1. (B-C) Orthophotos resulting from UAV survey at an altitude of 100 m and 50 m, respectively, in the same area as Figure 9A. Rose diagrams of opening directions measured through piercing points of Figures B and C are shown. (D) Scatter plots with opening direction vs. fracture dilation, referring to orthophotos shown in Figures. 9B (orange dots) and 9C (blue dots), respectively. (E) Field view and (F) aerial view by UAV survey (at altitude of 100 m) of the same tension fracture.*

### 4.3 Key area 3

Key area 3 has been UAV-surveyed at an elevation of 100 m: this resulted in a 8 cm resolution orthomosaic that covers an area of 8.1 km$^2$ (Fig. 11A). The analysis of this area is crucial for studying, for the first time, rift mechanisms in the 8-10 ka old lava units. We measured on the orthomosaic a total of 275 opening direction and dilation values along 260

fractures (Fig. 11A – Rose diagram). The average opening direction is N108.2° whereas the average strike of fractures corresponds to N13.9° (Fig. 11A) and dilation values range from 0.34 to 6.24 m. Spatial variations of opening direction and strike of fractures are shown in Figs. 11B-C-D-E. Figures 11B and 11D display the relation between opening directions, easting (Fig. 11B) and northing (Fig.11D): the range increases moving eastward, and the maximum value increases up to N140-150°. The same occurs in relation with northing (Fig. 11D): the range of opening directions is wider and reaches higher values (N132°) with the increasing of northing. Figures 11C and 11E show the relation of strike of fractures with easting (Fig. 11C) and northing (Fig. 11E). As for opening direction values, also in this case the strike of fractures reaches higher values (up to N42°) going eastward and northward, and the range of possible strike values is wider. The total extensional component measured along the 1.7-km-long white dashed line in Figure 11A is 24.33 m, corresponding to a stretch of 1.013.

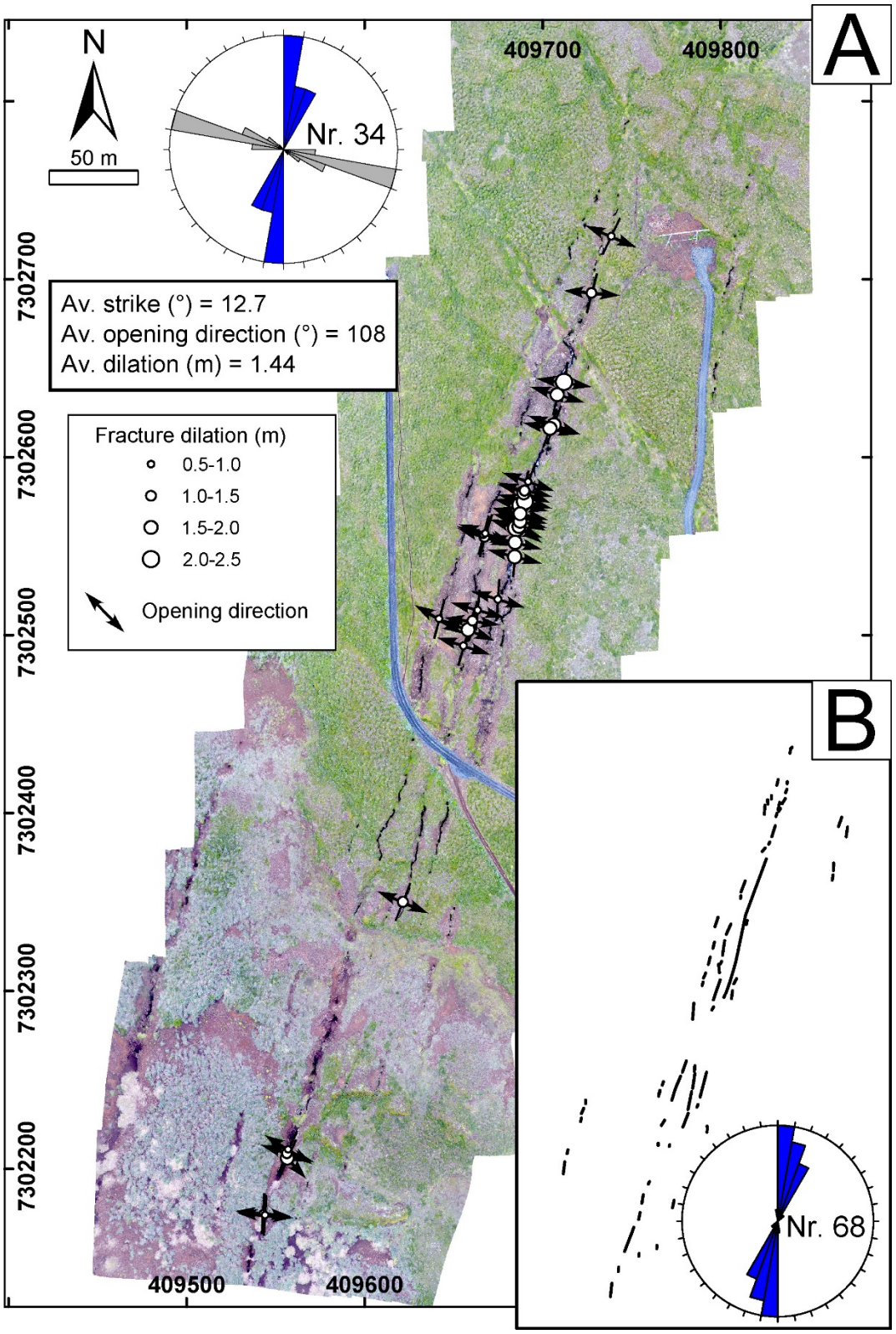


***Figure 10.*** *(A) Fracture dilation and opening directions measured on the 8-cm-resolution orthomosaic, related to Key area 2 and a flight elevation of 100 m. A total of 34 measures have been taken, as shown by the rose diagram in the upper left corner. Average fracture strike (blue in the rose diagram), average opening direction (grey) and average dilation (meters) are reported. (B) Sketch of fractures remotely traced on the 100 meters-elevation orthomosaic of Key area 2. Rose diagram shows strike values (68 total measures).*

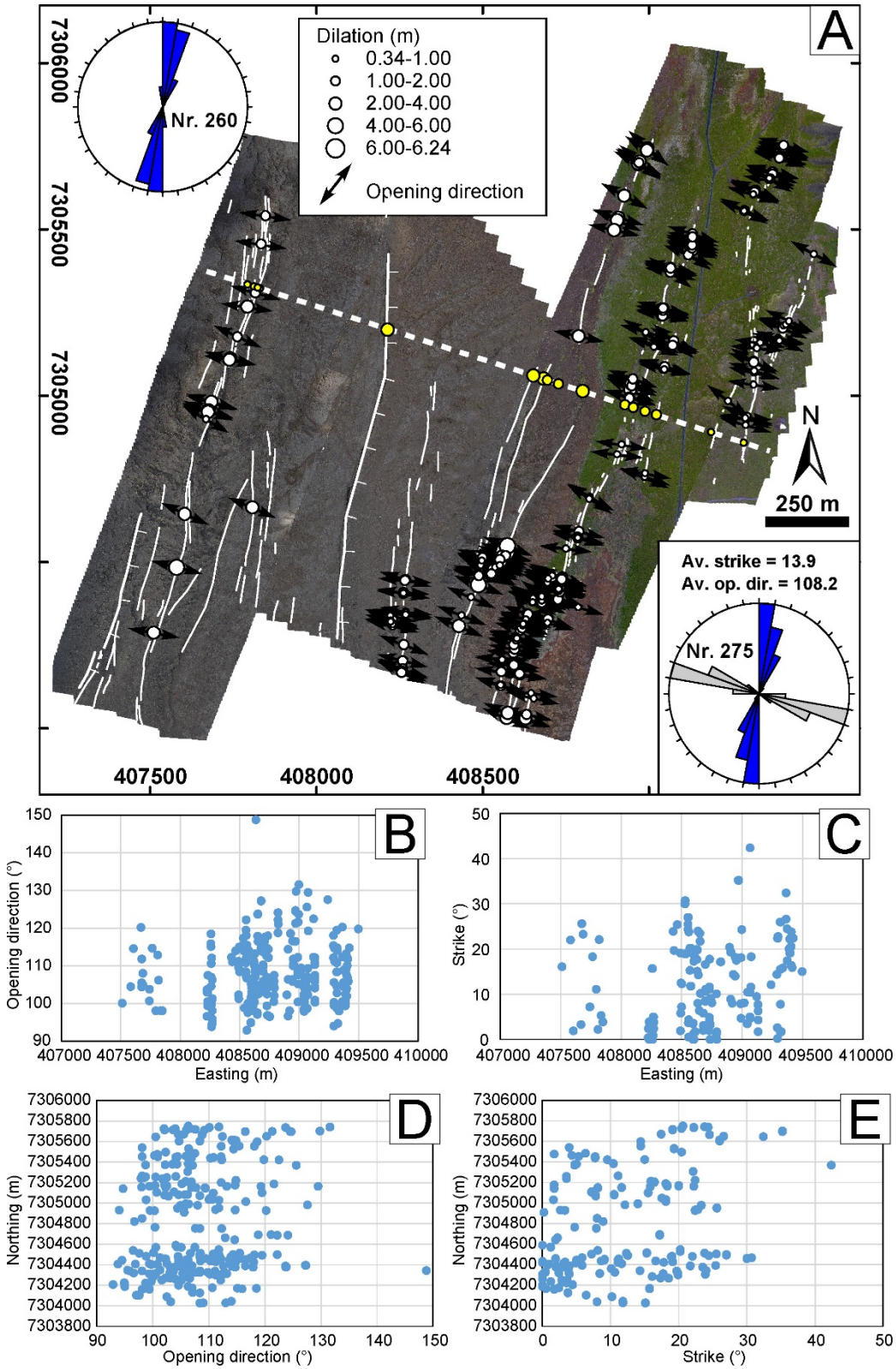


***Figure 11.*** *(A) Map of the 260 fractures (strike is reported in the upper right rose diagram) mapped on the 8-cm-resolution orthomosaic. Fracture dilation and opening directions were quantified at 275 sites. The rose diagram in the lower right corner report fracture strike (blue in the rose diagram) and corresponding opening direction (in grey). Faults and fractures are outlined in white, bars indicate downthrown block for normal faults. Graphs show fracture opening direction and strike vs. the easting (B-C) and the northing (D-E). Yellow dots represent locations where dilation has been quantified to calculate the stretch along the dashed whit line, oriented N108°.*

## 6. Discussion

### 6.1 Assessment of UAV surveys for active tectonics and volcano-tectonics

The use of UAV surveys in structural geology has been investigated in a few recent works. For example, Bemis et al. (2014) mapped ancient faults in Australia, whereas Vasuki et al. (2014) proposed a semi-automated method to map faults using photogrammetric data of rock exposures. Cawood et al. (2017) focused on bedding geometry of folds, by comparing Aerial Structure from Motion (ASfM) acquired from UAV surveys, LIDAR data and classical field surveys by compass. These authors concluded that ASfM achieved some divergence of measurements respect to direct field survey, but this divergence is significantly less than for terrestrial LiDAR and terrestrial SfM.

In our study instead, we compared two different methodologies to collect data at active volcano-tectonic and tectonic structures: field and UAV surveys. In order to define the most useful and efficient procedure, we remotely collected vertical offsets of faults and dilation and opening direction of tension fractures on the orthomosaics and DTMs generated by UAV surveys at 50 m and 100 m elevation. This allowed us to reconstruct the strain field of a wide area, as well as to quantify the stretch. The results prove the high reliability of the UAV approach for active tectonic purposes (Figs. 12A-B). In fact, the range of differences between measures of opening direction in the field and on 50-m-elevation orthomosaics is 1.8°-11°, whereas it is 1.4-12.9° in the case of 100-m-elevation (Fig. 12A). On the other hand, the range of differences between measures of dilation in the field and on UAV-derived 50-m-elevation orthomosaics is only 0.004-0.102 meters, whereas it is 0.002-0.152 meters if considering 100-m-elevation orthomosaics (Fig. 12B).

These data demonstrate that increasing the flight elevation (from 50 to 100 m) does not affect the accuracy and amount of collected measures: this is also shown by an increase of only one measure (in a specific case) on the orthomosaic associated with 50 m of elevation compared to the orthomosaic associated with 100 m (Figs. 9A-B-C). This observation is also supported by the scatterplot of Figure 12A: the trend lines associated

with the two different flight elevations (in terms of measures of opening direction) are almost identical. Our study proves that the use of UAV surveys is crucial for high-detailed structural-geological analysis of active tectonic and volcano-tectonic features: this new methodology provides a wider spatial coverage of the study area respect to fieldwork, the latter being also time-expensive. We choose 100 m as the best elevation for our purposes: a survey at this elevation takes less time (Table 2) and drains the battery less, giving the possibility to cover wider areas and to conclude more flights in the same work session.

The effectiveness of UAV-based surveys in terms of logistic is also shown by a comparison with field surveys by Pasquaré Mariotto et al. (2015) in the same rift zone: in that case, the authors were able to collect 92 measures in seven days of extensive fieldwork within an area of about 16 $km^2$ and a team composed by four persons. In our study, we were able to collect 359 measures by UAV surveys, quadrupling the amount of data, in just two days with a team composed only by two people.

We are aware that this methodology presents limits, such as the battery life and weather conditions that might limit the productivity of UAV surveys, but here we demonstrate the possibility and importance of covering very wide areas and to have a clear vision from the above of volcano-tectonic structures that might be very difficult to reach in the field, due to logistic conditions.

Furthermore, considering future applications, we highlight also that the high ground precision attained here, is consistent with the possibility of repeating UAV surveys of the same area at some years of distance, thus producing maps also of the present-day deformation field.

### 6.2 Fracture geometry, opening direction and dilation

The mapped 397 fractures strike between N-S and NE-SW, with the maximum frequency at N-S and NNE-SSW (rose diagram in Fig. 12C). The longest fractures, reaching up to 1173 meters in Key area 3, are in the range N4°-N28° (Figs. 11A and 12C), although

most of them are < 300 m. In general, Key areas 1 and 2 are characterized by shorter length of fractures respect to Key area 3 (Fig. 12C). As shown in Figures 5C-D and 11, some of them are associated with a vertical component and are classified as normal faults if they have a systematic and continuous vertical offset > 1 m. On the contrary, the fractures recognized without this characteristic, have been classified as tension fractures; in this case we measured opening direction and dilation (e.g. Figs. 4C-D). In all three key areas, the opening direction is about N108° (Figs. 7, 10 and 11A): lava deposits in Key areas 2 and 3 have an age of 8-10 ka, whereas rocks in Key area 1 have an age of 2.4 ka, suggesting that the overall spreading direction in the area can be the same for post-LGM age. Spreading direction in the NVZ is given as follows by different authors and methods. Hjartardóttir et al. (2012) suggested a spreading vector of N106° calculated from DeMets et al. (1994) who used geomagnetic data (up to 2.6 Ma - long-term data). DeMets et al. (2010) suggested a spreading vector of N104°, considering GPS and geological data (magnetic, bathymetric and earthquake data; up to 3.16 Ma - long-term data). Drouin et al. (2017) suggested a present-day spreading direction of N112° for the time window 2008-2014, basing on GPS data. Other authors who worked on the time windows 1997-2011 and 2006-2010, found out a spreading direction of N109° and N115°, respectively (Metzger et al., 2013; Metzger et al., 2011).

Our data cover a time window (Holocene times) that is much larger than GPS data but much smaller than the periods investigated by geomagnetic data. Hence, our data indicating N108° are very close to the previous long-term N106° results (DeMets et al., 1994). Overall fracture strike is mostly orthogonal to the spreading vector, as also suggested for the active KFS (Hjartardóttir et al., 2012) where fractures and eruptive fissures usually strike N to NNE. Local perturbation of opening direction can be related to possible dyke intrusion at a shallow depth, as shown by data reported in Ruch et al. (2016) for 2014-2015 Bárðarbunga dyking event. Furthermore, both fractures strike and opening direction in these

areas seem not to be influenced by strike-slip movements along the HFF, since they are further away than 500 m: at such distance, Tibaldi et al. (2016a) found a complex fractures geometry due to ThFS-HFF interaction. Always in regards to the opening direction, rose diagrams show that most opening occurs perpendicular to fracture strike (Figs. 7A, 10 and 11A) although left and right-lateral component are also present, with a predominance of the latter (Figs. 13A-B). In particular: *i)* 148 fractures have a lateral component < 5° (thus considered mainly extensional); *ii)* 170 fractures show a right-lateral component > 5° and are mainly in the range N0°-N25°; *iii)* just 42 fractures show a left-lateral component > 5° and are in the range of N15°-N30° (Fig. 13B). Based on all the above, we conclude that our spreading direction can represent the summa of multiple incremental events of crustal tectonic stretching under plate spreading, in combination with events of shallow dyking, as will be further detailed in the following chapter. On the contrary, GPS-inferred spreading directions (N109-115°), cover just few years/decades and represent a process of deformation more limited in time.

In regard to the extension amount, the stretching ratio calculated in Key area 3 is 1.013 over 1.7 km, measured on the white dashed line in Figure 11A; the total extensional component is 24.33 m. Dauteuil et al. (2001) estimated a stretching ratio of 1.009 along a transect located just north of the 1984 Krafla lava flow and a total extension of 30 m; such area provides an image of the deformation accumulated for the latest 10,000 ys. Differently, Paquet et al. (2007) calculated a stretching ratio of 1.036-1.046 across the Tertiary Alftafjordur dyke swarm, describing a deformation that lasted 1 Ma or more. Our stretching is more similar to the ratio estimated at Krafla, where it is very well known that both tectonic forces and magmatic forces (dyking) contributed to surficial deformations.

### 6.3 Origin of deformation

As well known, Iceland is an excellent natural laboratory to study the interactions between magmatic activity and extensional tectonics because of its location above the hot-spot and on a divergent plate margin (Paquet et al., 2007). Many researches here already demonstrated the relation between dyke injection and fissure swarms (Helgason and Zentilli, 1985; Forslund and Gudmundsson, 1991; Gudmundsson, 1995a; Tentler, 2005): fractures at the surface are the result of the emplacement of dyke swarms at depth, such as those in the Tertiary lava-pile of Iceland (Walker, 1965; Opheim and Gudmundsson, 1989; Tentler, 2005). Furthermore, the formation of a narrow graben at the surface should be induced by the upward advancement of the tip line of a shallow dyke below it (Pollard and Holzhausen, 1979; Bonafede and Olivieri, 1995).

These fractures in Iceland are seismically and geodetically highly active during rifting periods, which usually occur at time intervals of tens to a few hundred years, whereas they become inactive during inter-rifting stages (Hjartardóttir et al., 2016b). During rifting events, movement along fractures can occur in association with subsiding areas forming graben structures, fracture dilation and sometimes opening eruptive fissures. Such features have been observed both in Iceland rift zones as well as in the Eastern Africa Rift (e.g. Bjornsson et al., 1977; Abdallah et al., 1979; Tryggvason, 1984, 1994; Hamling et al., 2009; Wright et al., 2012). The intense earthquake activity associated with rifting migrates away from a rapidly subsiding volcanic centre (Einarsson, 1991; Einarsson and Brandsdottir, 1980), suggesting magma migration along dykes that can result in a subaerial eruption, as occurred in the well-documented cases of Krafla and Bardarbunga rifting episodes (Opheim and Gudmundsson, 1989; Hjartardóttir et al., 2012, 2016c; Sigmundsson et al., 2015; Gudmundsson et al., 2016). For example, most faults and tension fractures originated during the 1975-1984 Krafla rifting episode are the result of northward migration of magma as far as 30 km from the central volcano, forming dykes at shallow depth (1-4 km), as suggested by earthquake distribution and characteristics (Einarsson and Bransdottir, 1980).

On the other hand, even though dyking can accommodate partly or totally the stretching induced by regional extension, the effect of tectonics is equally crucial since formation of dykes is favoured at divergent plate boundaries (Sigmundsson et al., 2015). Detouil et al. (2007) suggested that fissuring and faulting have had a nearly equal role in accommodating the deformation for a period of 10,000 ys in the northern Krafla fissure swarm (KFS), whereas Hjartardóttir et al. (2012) observed a clear predominance of the regional tectonic stress field on the origin of extension, shown by eruptive fissures within Krafla central volcano being parallel to the fissure swarm. The prevailing role of tectonics in controlling the formation of tension fractures, which thus can originate before dykes inject, is also stated by Paquet et al. (2007), who noticed that eruptive fissures usually occur within the first ten of kilometres from the volcanic centres, whereas rarely-erupting open fissures can form farther away. To become eruptive, a dyke might also intersect at depth pre-existing open faults (Gudmundsson, 1992) or fissures. An example of the above process is shown by the recentmost 2014 Bardabunga rifting event, where a propagating dyke has been captured by the plate-spreading field when it was sufficiently far from the Bardarbunga central volcano, which is located to the west of the central axis of plate spreading (Sigmundsson et al., 2015).

To conclude, we highlight the presence of narrow grabens (Figs. 5C-D) and tension fractures, also associated to topographic bulging (Figs. 8C-D), which suggest a possible origin by dyke intrusion. Notwithstanding, there are also some structures that are not associated to bulging, as well as some normal faults have a preferential westward dip in the ThFS (e.g. Tibaldi et al., 2016a). These features, together with the observation that our areas of study are off-axis respect to the main axial plate spreading (Drouin et al., 2017), suggest that in addition to dyke intrusions, a contribution of far-field tectonic stresses linked to plate spreading cannot be excluded in fracture formation and enlarging.

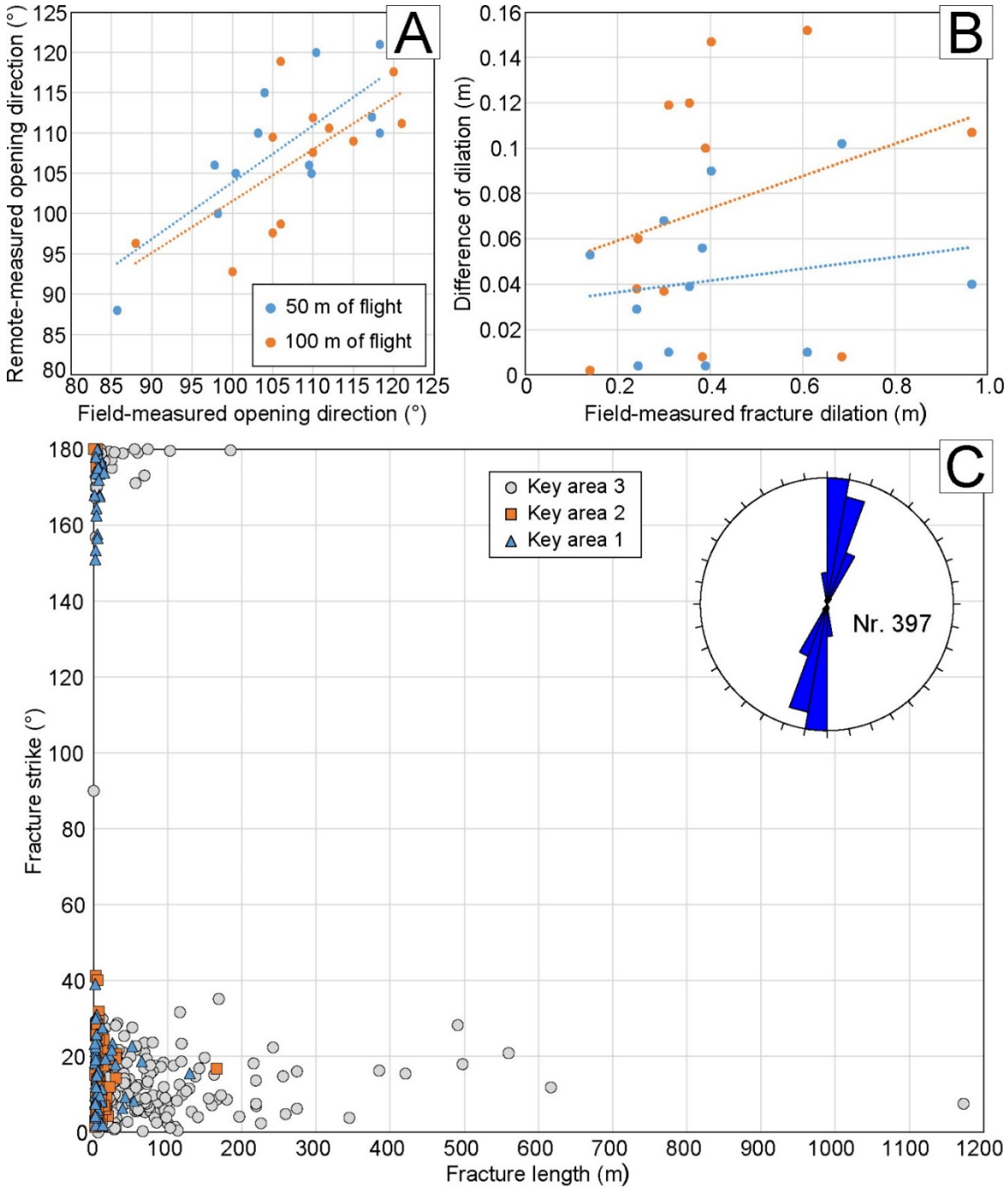


***Figure 12**. (A) Plot of opening directions measured in the field (x-axis) versus opening directions measured from orthomosaics derived from UAV surveys (y-axis) both at an elevation of 50 m and 100 m. (B) Plot of fracture dilation measured in the field (x-axis) versus the difference of fracture dilation between UAV and field data (y-axis), at both elevations. (C) Distribution of fracture length versus strike for the three key areas. Rose diagram of overall fracture strike is reported.*

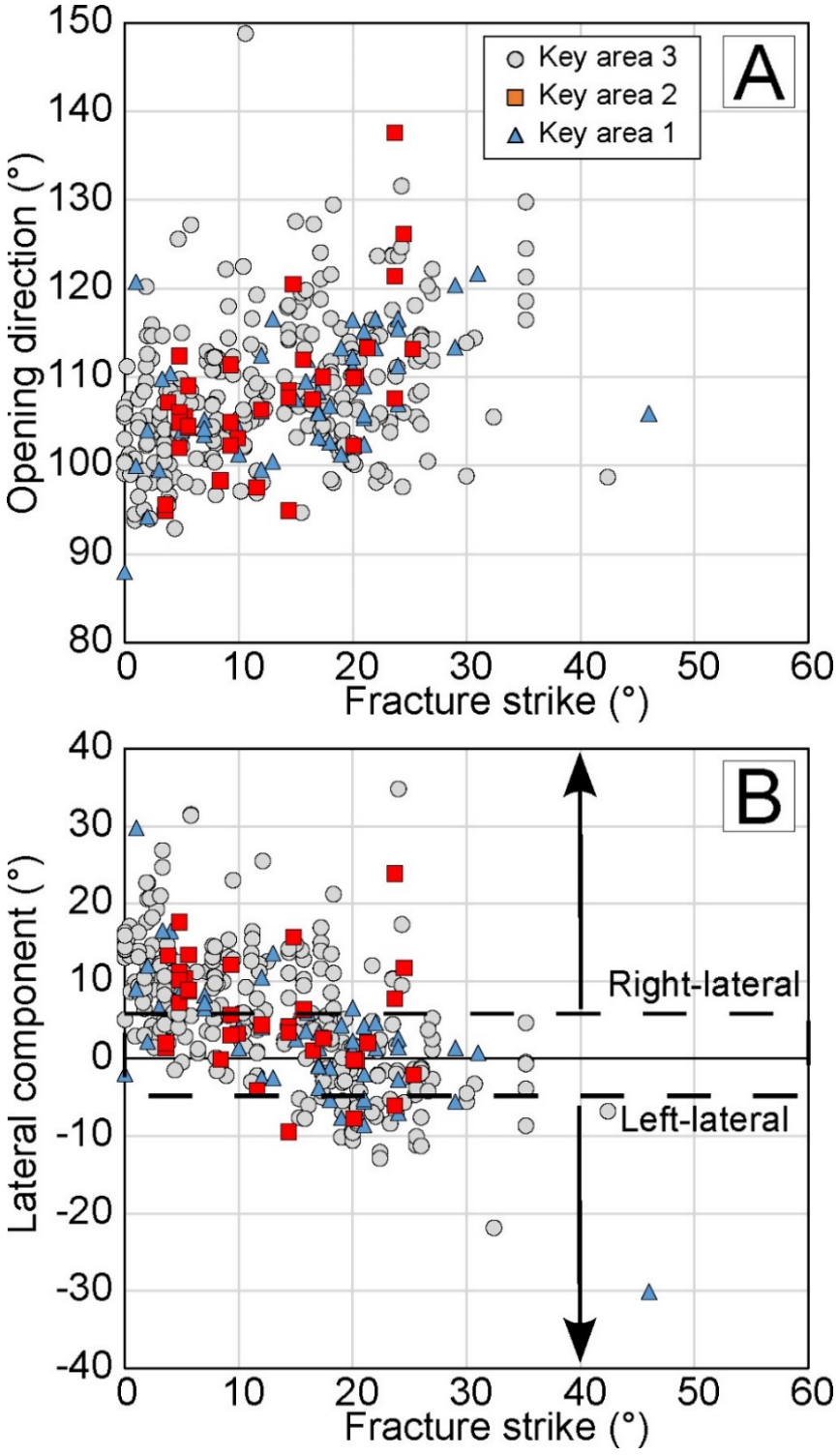


***Figure 13.*** *Shear components of fractures: (A) Fracture strike vs. opening direction, and (B) Fracture strike vs. right-lateral and left-lateral component. All three key areas are represented.*

## 7. Conclusions

We tested the use of UAV in order to identify the best practice to study Holocene deformations within the active ThFS (Northern Volcanic Zone of Iceland), in terms of tension fractures and normal faults.

We suggested a flight elevation of 100 m above the terrain as the most efficient to collect a large number of data with a suitable accuracy, saving plenty of time respect to only field activity, and as the best compromise between useful ground resolution, structural targets to be identified and measured, time spending, and UAV battery duration.

We defined the geometry and kinematics of 397 fractures, collecting 361 structural data. The resulting data set allowed to precisely quantify the overall direction of plate spreading at N108°, referred to Holocene times. The stretch calculated in the 8-10 ka old lava unit is 1.013. This deformation in the area can be related to both dyke intrusions and extensional tectonics.

By comparison with the structural data surveyed in the field, it resulted that UAV surveys allow to attain the same precision in quantifying the recent and active deformation field of a wide area. In comparison with the other methods, the use of a medium level UAV equipped with its standard commercial camera in the visible band of the electromagnetic spectrum, lets save plenty of time and funds reaching an adequate result for the scopes here illustrated.

**Acknowledgments**

This work is a contribution to the International Lithosphere Program - Task Force II and has also been carried out in the framework of ESA Project Nr. 38829. Funding for field work came from ILP and from the MIUR project ACPR15T4_00098 – Argo3D (http://argo3d.unimib.it/). This article is also an outcome of Project MIUR – Dipartimenti di Eccellenza 2018–2022.

**References**

Abdallah, A., Courtillot, V., Kasser, M., Le Dain, A. Y., Lépine, J. C., Robineau, B. & Tarantola, A. (1979). Relevance of Afar seismicity and volcanism to the mechanics of accreting plate boundaries. Nature, 282(5734), 17.

Ágústsdóttir, T., Woods, J., Greenfield, T., Green, R. G., White, R. S., Winder, T. & Soosalu, H. (2016). Strike-slip faulting during the 2014 Bárðarbunga-Holuhraun dike intrusion, central Iceland. Geophysical Research Letters, 43(4), 1495-1503.

Angster, S., Wesnousky, S., Huang, W.L., Kent, G., Nakata, T., & Goto, H., 2016. Application of UAV photography to refining the slip rate on the Pyramid Lake fault zone, Nevada. Bulletin of the Seismological Society of America, 106, 2, doi: 10.1785/0120150144.

Baiocchi, V., Dominici, D., Milone, M. V., & Mormile, M., 2013. Development of a software to plan UAVs stereoscopic flight: An application on post-earthquake scenario in L'Aquila city. In International Conference on Computational Science and Its Applications, Springer, Berlin, Heidelberg, 150-165.

Bemis, S.P., Micklethwaite, S., Turner, D., James, M.R., Akciz, S., Thiele, S.T., & Bangash, H.A., 2014. Ground-based and UAV-based photogrammetry: A multi-scale, high-resolution mapping tool for structural geology and paleoseismology. Journal of Structural Geology, 69, 163-178.

Björnsson, A., Saemundsson, K., Einarsson, P., Tryggvason, E., & Grönvold, K. (1977). Current rifting episode in north Iceland. Nature, 266(5600), 318.

Bi, H., Zheng, W., Ren, Z., Zeng, J., & Yu, J., 2017. Using an unmanned aerial vehicle for topography mapping of the fault zone based on structure from motion photogrammetry. International Journal of Remote Sensing, 38(8-10), 2495-2510.

Bonafede, M. and Olivieri, M. (1995). Displacement and gravity anomaly produced by a shallow vertical dyke in a cohesionless medium. Geophysical Journal International 123, 639-652.

Buckley, S.J., Schwarz, E., Terlaky, V., Howell, J.A., 2010. Combining aerial photogrammetry and terrestrial lidar for reservoir analog modeling. Photogrammetric Eng. Remote Sens. 76 (8), 953e963.

Cawood, A.J., Bond, C.E., Howell, J.A., Butler, R.W., & Totake, Y., 2017. LiDAR, UAV or compass-clinometer? Accuracy, coverage and the effects on structural models. Journal of Structural Geology, 98, 67-82.

Cembrano, J., & Lara, L. (2009). The link between volcanism and tectonics in the southern volcanic zone of the Chilean Andes: a review. Tectonophysics, 471(1-2), 96-113.

Darmawan, H., Walter, T.R., Brotopuspito, K.S., & Nandaka, I.G.M.A. (2018). Morphological and structural changes at the Merapi lava dome monitored in 2012–15 using unmanned aerial vehicles (UAVs). Journal of Volcanology and Geothermal Research, 349, 256-267.

Dauteuil, O., Angelier, J., Bergerat, F., Verrier, S., Villemin, T., 2001. Deformation partitioning inside a fissure swarm of the northern Icelandic rift. Journal of Structural Geology 23, 1359e1372.

Deffontaines, B., Chang, K. J., Champenois, J., Fruneau, B., Pathier, E., Hu, J.-C., Lu S.-T., &Liu, Y.C., 2016. Active interseismic shallow deformation of the Pingting terraces (Longitudinal Valley–Eastern Taiwan) from UAV high-resolution topographic data combined with InSAR time series. Geomatics, Natural Hazards and Risk, 1-17.

DeMets, C., Gordon, R. G., Argus, D. F., & Stein, S. (1994). Effect of recent revisions to the geomagnetic reversal time scale on estimates of current plate motions. Geophysical research letters, 21(20), 2191-2194.

Drouin, V., Sigmundsson, F., Ófeigsson, B. G., Hreinsdóttir, S., Sturkell, E., & Einarsson, P. (2017). Deformation in the Northern Volcanic Zone of Iceland 2008–2014: An interplay of tectonic, magmatic, and glacial isostatic deformation. Journal of Geophysical Research: Solid Earth, 122(4), 3158-3178.

Einarsson, P. (1991). Earthquakes and present-day tectonism in Iceland. Tectonophysics, 189(1-4), 261-279.

Einarsson, P., & Brandsdóttir, B. (1978). Seismological evidence for lateral magma intrusion during the July 1978 deflation of the Krafla volcano in NE-Iceland (No. UI-79-9-7). University of Iceland, Reykjavik, IS.

Favalli, M., Fornaciai, A., Nannipieri, L., Harris, A., Calvari, S., & Lormand, C. (2018). UAV-based remote sensing surveys of lava flow fields: a case study from Etna's 1974 channel-fed lava flows. Bulletin of Volcanology, 80(3), 29.

Fjäder, K., Gudmundsson, A., Forslund, T., 1994. Dikes, minor faults and mineral veins associated with a transform fault in North Iceland. Journal of Structural Geology, 16(1), 109-119.

Forslund, T., & Gudmundsson, A. (1991). Crustal spreading due to dikes and faults in southwest Iceland. Journal of Structural Geology, 13(4), 443-457.

Gao, M., Xu, X., Klinger, Y., van der Woerd, J., & Tapponnier, P., 2017. High-resolution mapping based on an Unmanned Aerial Vehicle (UAV) to capture paleoseismic offsets along the Altyn-Tagh fault, China. Scientific Reports, 7.

Garcia, S., Angelier, J., Bergerat, F., Homberg, C., 2002. Tectonic analysis of an oceanic transform fault zone revealed by fault–slip data and earthquake focal mechanisms: the Husavik–Flatey Fault, Iceland. Tectonophysics, 344, 157–174.

Gold, P.O., Cowgill, E., Kreylos, O., Gold, R.D., 2012. A terrestrial lidar-based workflow for determining three-dimensional slip vectors and associated uncertainties. Geosphere 8, 431-442.

Gong J.H., Wang D.C., Li Y., Zhang L.H., Yue Y.J., Zhou J.P., Song Y.Q., 2010. Earthquake induced geological hazard detection under hierarchical stripping classification framework in the Beichuan area. Landslides, 7(2), 181-9.

Gudmundsson, A. (1987). Geometry, formation and development of tectonic fractures on the Reykjanes Peninsula, southwest Iceland. Tectonophysics, 139(3-4), 295-308.

Gudmundsson, A., 1995. The geometry and growth of dykes. In: G. Baer and A. Heimann (eds.), Physics and Chemistry of Dykes. Rotterdam: Balkema, pp. 23–34.

Gudmundsson, A. (1992). Formation and growth of normal faults at the divergent plate boundary in Iceland. Terra Nova, 4(4), 464-471.

Gudmundsson, A., Brynjólfsson, S., Jónsson, M. Th., 1993. Structural analysis of a transform fault-rift zone junction in North Iceland. Tectonophysics, 220, 205–221.

Gudmundsson, A. (2007). Infrastructure and evolution of ocean-ridge discontinuities in Iceland. Journal of Geodynamics, 43(1), 6-29.

Gudmundsson, M. T., Jónsdóttir, K., Hooper, A., Holohan, E. P., Halldórsson, S. A., Ófeigsson, B. G., et al., (2016). Gradual caldera collapse at Bárdarbunga volcano, Iceland, regulated by lateral magma outflow. Science, 353(6296), aaf8988.

Hamling, I. J., Ayele, A., Bennati, L., Calais, E., Ebinger, C. J., Keir, D. and Yirgu, G. (2009). Geodetic observations of the ongoing Dabbahu rifting episode: new dyke intrusions in 2006 and 2007. Geophysical Journal International, 178(2), 989-1003.

Helgason, J., & Zentilli, M. (1985). Field characteristics of laterally emplaced dikes: Anatomy of an exhumed Miocene dike swarm in Reydarfjördur, eastern Iceland. Tectonophysics, 115(3-4), 247-274.

Hjartardóttir, Á.R. (2012). The fissure swarm of the Askja central volcano (Doctoral dissertation).

Hjartardóttir, Á.R., Einarsson, P., Björgvinsdóttir, S.G., 2016a. Fissure swarms and fracture systems within the Western Volcanic Zone, Iceland–Effects of spreading rates. Journal of Structural Geology, 91, 39-53.

Hjartardóttir, Á. R., Einarsson, P., Magnúsdóttir, S., Björnsdóttir, Þ., & Brandsdóttir, B. (2016b). Fracture systems of the Northern Volcanic Rift Zone, Iceland: an onshore part of the Mid-Atlantic plate boundary. Geological Society, London, Special Publications, 420(1), 297-314.

Hjartardóttir, Á. R., Einarsson, P., Gudmundsson, M. T., & Högnadóttir, T. (2016c). Fracture movements and graben subsidence during the 2014 Bárðarbunga dike intrusion in Iceland. Journal of Volcanology and Geothermal Research, 310, 242-252.

Hu J.P., Wu W.B., Tan Q.L., 2012. Application of unmanned aerial vehicle remote sensing for geological disaster reconnaissance along transportation lines: a case study. Appl. Mech. Mat., 226, 2376–2379.

James, M.R., Robson, S., 2012. Straightforward reconstruction of 3D surfaces and topography with a camera: accuracy and geoscience application. J. Geophys. Res., 117, F03017. http://dx.doi.org/10.1029/2011JF002289.

James, M.R., Robson, S., d'Oleire-Oltmanns, S., Niethammer, U., 2017. Optimising UAV topographic surveys processed with structure-from-motion: ground control quality, quantity and bundle adjustment. Geomorphology 280, 51-66.

Jiao, Q., Jiang, W., Zhang, J., Jiang, H., Luo, Y., & Wang, X., 2016. Identification of paleoearthquakes based on geomorphological evidence and their tectonic implications for the southern part of the active Anqiu–Juxian fault, eastern China. Journal of Asian Earth Sciences, 132, 1-8.

Johnson, K., Nissen, E., Saripalli, S., Arrowsmith, J. R., McGarey, P., Scharer, K., Williams, P., & Blisniuk, K., 2014. Rapid mapping of ultrafine fault zone topography with structure from motion. Geosphere, 10(5), 969-986.

Magnúsdóttir, S., Brandsdóttir, B., 2011. Tectonics of the Þeistareykir fissure swarm. Jökull, 61, 65-79.

Marino C.M. & Tibaldi A., 1988. Use of Landsat and Seasat data as a tool in kinematic analysis: The Tunisian Atlas. International Journal of Remote Sensing, 9, 10-11, 1659-1673.

McCalpin, J. (Ed.) 1996. Paleoseismology, Vol. 62, Academic press, 588 pages.

Müller D., Walter T.R., Schöpa A., Witt T., Steinke B., Gudmundsson M.T. and Dürig T., 2017. High-resolution digital elevation modeling from TLS and UAV campaign reveals structural complexity at the 2014/2015 Holuhraun eruption site, Iceland. Front. Earth Sci., 5:59, doi: 10.3389/feart.2017.00059.

Opheim, J.A., Gudmundsson, A. (1989). Formation and geometry of fractures, and related volcanism, of the Krafla fissure swarm, northeast Iceland. Geological Society of America Bulletin, 101(12), 1608-1622.

Paquet, F., Dauteuil, O., Hallot, E., & Moreau, F. (2007). Tectonics and magma dynamics coupling in a dyke swarm of Iceland. Journal of Structural Geology, 29(9), 1477-1493.

Pasquarè Mariotto F., F.L. Bonali, A. Tibaldi, D. Rust, P. Oppizzi, A. Cavallo, 2015. Holocene displacement field at an emerged oceanic transform-ridge junction: The Husavik-Flatey Fault - Gudfinnugja Fault system, North Iceland. Journal of Structural Geology, 75, 118-134.

Pollard, D. D. and Holzhausen, G. (1979) On the mechanical interaction between a fluid-tilled fracture and the Earth's surface. Tectonophysics, 53, 27-57.

Ramli, M.F., Yusof, N., Yusoff, M.K., Juahir, H., & Shafri, H. Z.M., 2010. Lineament mapping and its application in landslide hazard assessment: a review. Bulletin of engineering Geology and the Environment, 69(2), 215-233.

Rathje, E. M., & Franke, K., 2016. Remote sensing for geotechnical earthquake reconnaissance. Soil Dynamics and Earthquake Engineering, 91, 304-316.

Saemundsson, K., 1974. Evolution of the axial rifting zone in northern Iceland and the Tjornes fracture zone. Geol. Soc. Am. Bull., 85, 495-504.

Saemundsson, K., Hjartarson, A., Kaldal, I., Sigurgeirsson, M.A., Kristinsson, S.G., Vikingsson, S., 2012. Geological map of the Northern Volcanic Zone, Iceland. Northern Part 1: 100.000. Reykjavik: Iceland GeoSurvey and Landsvirkjun.

Sigmundsson, F., Hooper, A., Hreinsdóttir, S., Vogfjörd, K. S., Ófeigsson, B. G., Heimisson, E.R. & Drouin, V. (2015). Segmented lateral dyke growth in a rifting event at Bárðarbunga volcanic system, Iceland. Nature, 517(7533), 191.

Stal, C., Bourgeois, J., De Maeyer, P., De Mulder, G., De Wulf, A., Goossens, R., Hendrickx, M., Nuttens, T., Stichelbaut, B., (2012). Test case on the quality analysis of structure from motion in airborne applications. In 32nd EARSeL Symposium: Advances in geosciences. European Association of Remote Sensing Laboratories (EARSeL).

Sturzenegger, M., Stead, D., 2009. Quantifying discontinuity orientation and persistence on high mountain rock slopes and large landslides using terrestrial remote sensing techniques. Nat. Hazards Earth Syst. Sci. 9 (2), 267-287.

Tentler, T. (2005). Propagation of brittle failure triggered by magma in Iceland. Tectonophysics, 406(1-2), 17-38.

Tibaldi A., 2015. Structure of volcano plumbing systems: A review of multi-parametric effects. J. Volcanol. Geotherm. Res., 298, 85–135.

Tibaldi, A. & Ferrari, L., 1991. Multisource remotely-sensed data, field checks and seismology for the definition of active tectonics in the Ecuadorian Andes. International Journal of Remote Sensing, 12, 2343-2358.

Tibaldi, A., & Bonali, F. L. (2018). A model to explain joint patterns found in ignimbrite deposits. Bulletin of Volcanology, 80(3), 26.

Tibaldi, A., & Bonali, F. L. (2018). Contemporary recent extension and compression in the central Andes. Journal of Structural Geology, 107, 73-92.

Tadini, A., Bonali, F. L., Corazzato, C., Cortés, J. A., Tibaldi, A., & Valentine, G. A. (2014). Spatial distribution and structural analysis of vents in the Lunar Crater Volcanic Field (Nevada, USA). Bulletin of Volcanology, 76(11), 877.

Tibaldi, A., Bonali, F.L., & Pasquaré Mariotto, F., 2016a. Interaction between transform faults and rift systems: a combined field and experimental approach. Frontiers in Earth Science, 4, 33.

Tibaldi, A., Bonali, F.L., Einarsson, P., Hjartardóttir, Á.R., & Pasquaré Mariotto, F., 2016b. Partitioning of Holocene kinematics and interaction between the Theistareykir Fissure Swarm and the Husavik-Flatey Fault, North Iceland. Journal of Structural Geology, 83, 134-155.

Tryggvason, E. (1984). Widening of the Krafla fissure swarm during the 1975–1981 volcano-tectonic episode. Bulletin volcanologique, 47(1), 47-69.

Tryggvason, E. (1994). Surface deformation at the Krafla volcano, North Iceland, 1982–1992. Bulletin of Volcanology, 56(2), 98-107.

Turner, D., Lucieer, A., & Watson, C., 2012. An automated technique for generating georectified mosaics from ultra-high resolution unmanned aerial vehicle (UAV)imagery, based on structure from motion (SfM) Point clouds. Remote Sens., 4, 1392-1410.

Vasuki, Y., Holden, E. J., Kovesi, P., & Micklethwaite, S. (2014). Semi-automatic mapping of geological Structures using UAV-based photogrammetric data: An image analysis approach. Computers & Geosciences, 69, 22-32.

Walker, G. P. L. (1965). Evidence of crustal drift from Icelandic geology. Phil. Trans. R. Soc. Lond. A, 258(1088), 199-204.

Walter, T. R., Jousset, P., Allahbakhshi, M., Witt, T., Gudmundsson, M. T., & Hersir, G. P. (2018). Underwater and drone based photogrammetry reveals structural control at Geysir geothermal field in Iceland. Journal of Volcanology and Geothermal Research.

Westoby, M.J., Brasington, J., Glasser, N.F., Hambrey, M.J., Reynolds, J.M., 2012. “Structure-from-Motion” photogrammetry: a low-cost, effective tool for geoscience applications. Geomorphology 179, 300-314.

Wise, D.U., Funiciello, R., Parotto, M., & Salvini, F., 1985. Topographic lineament swarms: clues to their origin from domain analysis of Italy. Geological Society of America Bulletin, 96(7), 952-967.

Wright, T. J., Sigmundsson, F., Pagli, C., Belachew, M., Hamling, I. J., Brandsdóttir, B. and Einarsson, P. (2012). Geophysical constraints on the dynamics of spreading centres from rifting episodes on land. Nature Geoscience, 5(4), 242.

Wu, F., Ran, Y., Xu, L., Cao, J., & Li, A., 2017. Paleoseismological Study of the Late Quaternary Slip-rate along the South Barkol Basin Fault and Its Tectonic Implications, Eastern Tian Shan, Xinjiang. Acta Geologica Sinica (English Edition), 91(2), 429-442.